

Earth's Future

RESEARCH ARTICLE

10.1029/2023EF004037

Key Points:

- Grassland greening and enhanced water resource availability may coexist in most of NCTP in a warming climate
- Effects of plant physiological and hydrological factors along grassland greening on water yield in the future were analyzed
- The positive influence of enhanced water resource availability and ongoing grassland greening on future livestock production was quantified

Supporting Information:

Supporting Information may be found in the online version of this article.

Correspondence to:

D. Long and T. Liu,
dlong@tsinghua.edu.cn;
txliu1966@163.com

Citation:

Zhang, C., Long, D., Liu, T., Slater, L. J., Wang, G., Zuo, D., et al. (2023). Grassland greening and water resource availability may coexist in a warming climate in Northern China and the Tibetan Plateau. *Earth's Future*, *11*, e2023EF004037. <https://doi.org/10.1029/2023EF004037>

Received 15 AUG 2023

Accepted 22 NOV 2023

Author Contributions:

Conceptualization: Caijin Zhang, Di Long, Tingxi Liu






Data curation: Caijin Zhang, Di Long, Tingxi Liu

Formal analysis: Caijin Zhang, Di Long

Funding acquisition: Di Long

© 2023 The Authors. Earth's Future published by Wiley Periodicals LLC on behalf of American Geophysical Union. This is an open access article under the terms of the [Creative Commons Attribution-NonCommercial-NoDerivs License](https://creativecommons.org/licenses/by/4.0/), which permits use and distribution in any medium, provided the original work is properly cited, the use is non-commercial and no modifications or adaptations are made.

Grassland Greening and Water Resource Availability May Coexist in a Warming Climate in Northern China and the Tibetan Plateau

Caijin Zhang¹ , Di Long¹ , Tingxi Liu^{2,3} , Louise J. Slater⁴ , Guoqiang Wang⁵ , Depeng Zuo⁶, Limin Duan^{2,3}, Yanhong Cui¹, and Yingjie Cui¹

¹State Key Laboratory of Hydrosience and Engineering, Department of Hydraulic Engineering, Tsinghua University, Beijing, China, ²Water Conservancy and Civil Engineering College, Inner Mongolia Key Laboratory of Water Resource Protection and Utilization, Inner Mongolia Agricultural University, Hohhot, China, ³Collaborative Innovation Center for Integrated Management of Water Resources and Water Environment in the Inner Mongolia Reaches of the Yellow River, Hohhot, China, ⁴School of Geography and the Environment, University of Oxford, Oxford, UK, ⁵Center for Geodata and Analysis, Faculty of Geographical Science, Beijing Normal University, Beijing, China, ⁶Beijing Key Laboratory of Urban Hydrological Cycle and Sponge City Technology, College of Water Sciences, Beijing Normal University, Beijing, China

Abstract Greening of Northern China and the Tibetan Plateau (NCTP) has been observed by increases in the remotely sensed leaf area index (LAI), driven primarily by CO₂ fertilization effects, anthropogenic warming, and the implementation of ecological restoration programs. Continued growth of LAI throughout the 21st century is also projected by the Coupled Model Intercomparison Project Phase 6 (CMIP6) scenarios. However, the question of whether local water resources can sustain ongoing grassland greening has not been adequately investigated. Here we assessed the sustainability of water resources under grassland greening across NCTP under various climate scenarios using water yield (WY, defined as precipitation minus actual evapotranspiration) as the key metric. Unexpectedly, we observe the coexistence of increases in LAI and WY in most of NCTP. In a warming climate with increasing precipitation and CO₂, we find that grasses maintain high water use efficiency to sustain their growth, contributing to continued local water resource availability. Thus, livestock production may also continue to increase under the simultaneous growth of LAI and WY in the future.

Plain Language Summary The greening of Northern China and the Tibetan Plateau (NCTP) has been observed through increases in remotely sensed leaf area index (LAI), driven primarily by ecological restoration programs, climate change, and CO₂ fertilization effects. While continued growth of LAI throughout the 21st century is projected by Coupled Model Intercomparison Project Phase 6 (CMIP6) scenarios, there is limited understanding of whether local water resources may sustain the ongoing process of grassland greening in the context of more frequent and severe drought conditions under global warming. Using three schemes considering plant physiological and hydrological feedbacks toward climate change, our study unveils changes in regional water sustainability (i.e., water yield) under grassland greening across NCTP over the past four decades and up to the end of the 21st century. Surprisingly, we observe the coexistence of future grassland greening and enhanced water resource availability in most of NCTP. Moreover, increased precipitation from atmospheric transport and evaporation recycling, coupled with a warming climate and rising CO₂ levels, enables grasses to maintain high water use efficiency, sustaining their growth and contributing to the availability of local water resources. Additionally, projections suggest that the area occupied by livestock production across NCTP may continue to grow due to the simultaneous improvement in grassland and water resource availability.

1. Introduction

Grasslands account for approximately 30% of the global land surface (Lemaire et al., 2011) and possess critical ecosystem functions (e.g., regulating water cycles, storing carbon, controlling erosion, and providing livelihoods for living things) (Bengtsson et al., 2019). In China, nearly 40% of the land is covered by grasslands, 78% of which is distributed in Northern China and the Tibetan Plateau (NCTP) (Chen & Wang, 2000). Since the 1950s, desertification has been widespread in such arid and semi-arid regions. Wind erosion and freeze-thaw erosion are the main climate drivers of grassland degradation, whereas the cultivation of crops or pine trees and overgrazing are the main anthropogenic drivers (Bardgett et al., 2021; Li, C et al., 2021). Since 1978, to mitigate desertification, large ecological projects (such as the Three-North Shelter Forest Program and the Grain for Green Program)

Investigation: Caijin Zhang, Di Long, Tingxi Liu, Louise J. Slater, Guoqiang Wang, Depeng Zuo, Limin Duan, Yanhong Cui, Yingjie Cui

Methodology: Caijin Zhang, Di Long

Project Administration: Di Long

Resources: Caijin Zhang, Di Long,

Tingxi Liu, Louise J. Slater, Guoqiang

Wang, Depeng Zuo, Limin Duan,

Yanhong Cui, Yingjie Cui

Software: Caijin Zhang, Di Long

Supervision: Di Long

Validation: Caijin Zhang, Di Long,

Tingxi Liu

Visualization: Caijin Zhang, Di Long

Writing – original draft: Caijin Zhang,

Di Long, Louise J. Slater

Writing – review & editing: Caijin

Zhang, Di Long, Louise J. Slater

have been implemented across the NCTP region (Li, C et al., 2021; Lu, F et al., 2018). The degradation trend was reversed over the past two decades (Bryan et al., 2018), and the greening of NCTP has been observed by the increasing remotely sensed leaf area index (LAI) (Chen, C et al., 2019; Piao et al., 2020). Widespread greening has been driven mostly by CO₂ fertilization effects (Piao et al., 2020; Zhu et al., 2016) and large-scale ecological restoration (Jiang, P et al., 2022; Niu et al., 2019), but has also been affected by increases in warming and precipitation (Maina et al., 2022).

LAI projections under multiple scenarios of the Coupled Model Intercomparison Project (CMIP) indicate continued grassland greening throughout the 21st century (Piao et al., 2020). However, such greening may threaten the sustainability of water resources in these drylands (where actual evapotranspiration (ET_a) may account for more than 90% of precipitation (Pilgrim et al., 1988)) by inducing greater water consumption through ET_a (Lu, J et al., 2021; Yu et al., 2021). During the historical period, grassland greening in NCTP was supported mostly by increased precipitation (Miao, L et al., 2021; Zhao, W et al., 2020). However, drought conditions in Northern China are projected to become more frequent and severe under global warming (Miao, L J et al., 2020; Su, B et al., 2021), with increasing impacts of droughts on ecosystem stability in drylands (Zhang, Y et al., 2022). Therefore, the question of whether regional water resources can sustain ongoing grassland greening needs to be investigated.

Recent studies have focused on the historical effects of vegetation greening on the sustainability of water resources, with limited research on future possible changes. It is shown that grassland greening has reduced the sustainability of regional water resources (Bai et al., 2020; Li, J et al., 2017; Zhao, M et al., 2021), using scenarios with and without grassland greening, based on hydrological models or standalone ET_a estimation methods (Lan et al., 2021; Zhang, J et al., 2022; Zhao, M et al., 2021). However, the interplay between vegetation greening and water resource sustainability is complex and the influence of increasing water use efficiency (Pastore et al., 2019) (i.e., WUE, the ratio of gross primary production (GPP) and ET_a) and intensified evaporation recycling accompanied by greening (Hoek Van Dijke et al., 2022) also needs to be considered.

Drought events and continuously elevated atmospheric CO₂ tend to force vegetation to reduce excess water losses through partially closing stomata, thus increasing WUE (Pastore et al., 2019; Skelton et al., 2015). Such plant physiological feedback has the potential to alleviate the water stress caused by increasing LAI. Factors including climate warming, increased drought events, and elevated CO₂ that drive the above physical reactions are likely to persist in the future; therefore, increased WUE should be considered in any projections of future water resource availability. In addition, increased ET_a induced by greening would contribute to local and downwind precipitation (i.e., evaporation recycling), with varying effects on water yield (i.e., WY, defined as precipitation minus ET_a) in these areas (Piao et al., 2020; Zeng et al., 2018). Evaporation recycling alone may induce higher WY, especially in drylands (Zhou et al., 2021), while the combined influence of Earth's greening and evaporation recycling may even reverse such positive effects on regional water resources in drylands (i.e., decreasing WY) (Zeng et al., 2018). This complex hydrological feedback involved in the context of grassland greening should not be ignored, because ongoing greening is likely to continue intensifying evaporation recycling (Cui et al., 2022; Wang, X et al., 2021; Zeng et al., 2018).

Here we used WY to assess the sustainability of water resources under the effect of continued grassland greening in NCTP during 1982–2100, with an experimental design combining diagnostic and prognostic models for ET_a estimation. Diagnostic ET_a models that do not rely on precipitation as input have been shown to better retrieve historical ET_a and employ different mechanisms compared to prognostic models (Yilmaz et al., 2014). Comparison between diagnostic and prognostic model-based ET estimates and their combination can therefore be informative for the analysis of WY. The relatively independent diagnostic Penman-Monteith (PM) method (Allen et al., 1998) was applied to obtain ET_a estimates for the entire study period (during 1982–2100), primarily influenced by atmospheric water demand and vegetation greening. To estimate the competing effects of greening, increased WUE, and intensified evaporation recycling on WY during 2019–2100, two other ET_a schemes based on CMIP6 (the latest phase of the CMIP) projections across NCTP were used (i.e., prognostic estimates). To reflect future changes in livestock production under grassland greening, stocking herbivore numbers in four major provinces of NCTP were projected, given changes in the natural grazing environment. We assess how WY is projected to evolve across NCTP throughout the 21st century under the combined effects of vegetation greening, increased WUE, and intensified evaporation recycling, considering plant physiological and hydrological feedbacks. These projections could help facilitate grassland management globally and provide insights into whether grassland restoration is subject to water resource availability.

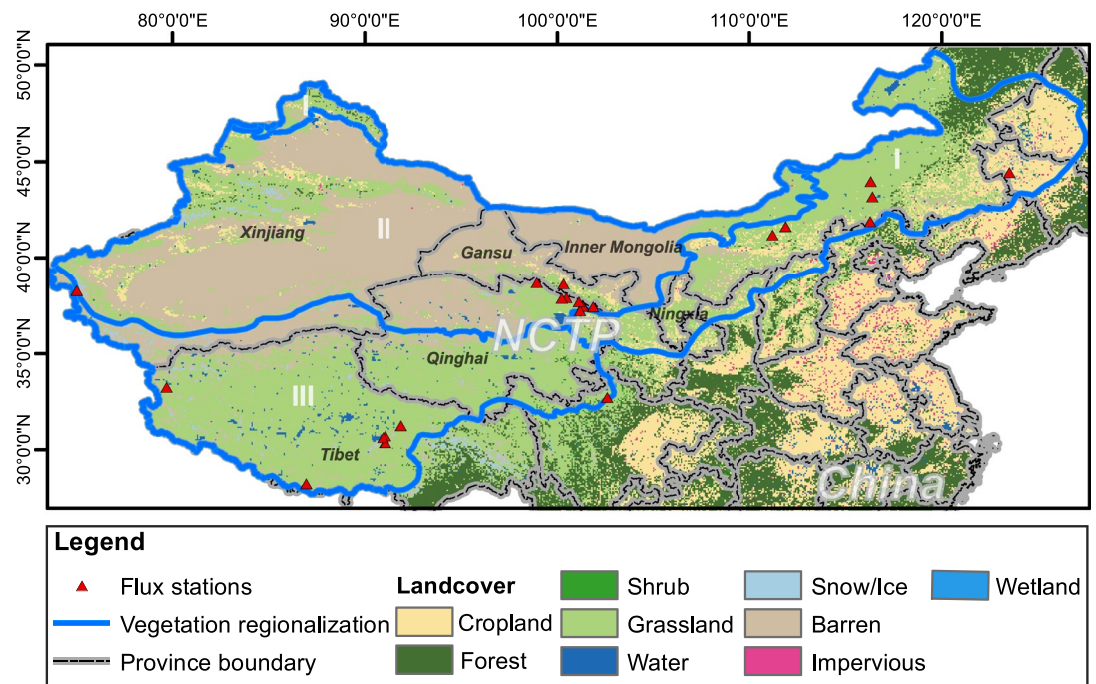


Figure 1. Boundaries of three grassland vegetation regions (Su, Y et al., 2020) in NCTP and locations of 25 flux stations. The background shows land cover data (CLCD) (Yang & Huang, 2021) in NCTP and its surrounding areas in the year 2000, as well as boundaries of six main provinces (gray outlines).

2. Materials and Methods

2.1. Study Area

Here we focus on the effects of grassland greening, increased WUE, and intensified evaporation recycling on historical and future WY across NCTP (Figure 1). China land cover data (CLCD) (Yang & Huang, 2021) show that grassland (~50%) is the dominant land cover across the entire NCTP region, followed by barren land (~30%) and cropland (~10%). According to grassland types from the digitized 1:1 million vegetation atlas of China (Su, Y et al., 2020), the NCTP region can be divided into three sub-regions (Figure 1), based on the dominant vegetation type, that is, temperate grassland (region I), temperate desert (region II), and alpine vegetation of the Qinghai-Tibet Plateau (region III). Typical steppe and sandy grassland are the major grassland ecosystems for region I, and alpine meadow and alpine steppe are the main grassland types for region III, whereas region II is covered mostly by temperate desert steppe (Li, L et al., 2020). Most grasslands are located in drylands with an aridity index below 0.65 (Li, C et al., 2021), where regional water resources are vital for plant biodiversity and ecosystems.

2.2. Data for Estimating Water Yield During 1982–2018

During 1982–2018, WY (at the daily timescale and 0.07° spatial resolution) was calculated using precipitation from the China meteorological forcing dataset (CMFD) (Yang et al., 2019) and ET_a estimated by the diagnostic PM model. The PM model requires climate forcing data, LAI, and land cover as inputs, listed in Table 1. CMFD daily climatic forcing data during 1982–2018 were used. The GLASS LAI during 1982–2014 (Xiao et al., 2016) and GLOBMAP LAI during 2001–2018 (Liu, Y et al., 2012) were used at an 8-day temporal resolution. GLASS LAI over the period 1982–2000 was corrected for each pixel by deducting the mean annual difference between the two datasets during 2001–2014. The two datasets were then resampled to the daily timescale based on the spatio-temporal linear interpolation method (Zhang, C et al., 2021). The CLCD land cover map (Yang & Huang, 2021) in 1985 was used to represent the land cover during 1982–1989, and the CLCD land cover maps in the corresponding year were used for the period from 1990 to 2018. In addition, historical WUE (used in the projection of GPP-based ET_a during the future period) was calculated from GLASS GPP and PM ET_a . Furthermore, historical

Table 1
List of Datasets During 1982–2100 Used for Estimating ET_a and WY in This Study

	Data set	Variable	Spatiotemporal resolution	Time span	Reference
Historical	CMFD	Precipitation	0.1°, daily	1982–2018	He et al. (2020)
		Air temperature, surface pressure, specific humidity, wind speed, downward solar radiation			
	GLASS	Leaf area index (LAI)	0.05°, 8-day	1982–2014	Xiao et al. (2016)
	GLOBMAP	LAI	0.07°, 8-day	2001–2018	Liu, Y et al. (2012)
	CLCD	Land cover	30 m, yearly	1985, 1990–2019	Yang & Huang, 2021
Future	GLASS	Gross primary production (GPP)	0.05°, 8-day	1982–2018	Liang et al. (2021)
	CMIP6	Precipitation	Different spatial resolutions for 14 models, monthly	2015–2100	Eyring et al. (2016)
		ET_a			
		Air temperature, surface pressure, specific humidity, wind speed, downward solar radiation, LAI			
GPP	Different spatial resolutions for 9 models, monthly				

variables (including climatic forcing data, LAI, precipitation, ET_a , and GPP) during 2015–2018 were used for bias correction of the corresponding CMIP6 variables.

2.3. Data for Projecting Water Yield During 2019–2100

During 2019–2100, WY was projected using the bias-corrected CMIP6 precipitation (denoted as CMIP6-based precipitation) and three ET_a schemes (i.e., PM ET_a , GPP-based ET_a , and CMIP6-based ET_a , see Section 2.5). Projected WY was obtained at the monthly timescale and $\sim 0.94^\circ$ spatial resolution. CMIP6 (Eyring et al., 2016) outputs, including meteorological (e.g., precipitation and air temperature), land surface (i.e., LAI and GPP), and hydrological variables (i.e., ET_a) were used, listed in Table 1. CMIP6 projected data from 15 general circulation models (GCMs, Table S1 in Supporting Information S1) under future scenario experiments during 2015–2100 were used, with output during 2015–2018 used for bias correction. Shared socioeconomic pathways 1, 2, and 5 and representative concentration pathways 2.6, 4.5, and 8.5 were selected from the Scenario Model Intercomparison Project, and denoted as the SSP126, SSP245, and SSP585 scenarios, respectively. In addition, CMIP6 projected LAI and climatic forcing data at the monthly timescale were used to generate ET_a with the PM model. Note that land cover is assumed to remain constant during the future period, so the CLCD land cover map for 2019 was used in the PM modeling for the period 2019–2100. This is because according to projected land cover fractions of most CMIP6 models (seven out of eight models shown in Table S1 in Supporting Information S1), maximum changes in land cover for grassland, barren, and crop between 2100 and 2019 only account for 2.5%, 1.5%, and 1.7% of the entire NCTP region, respectively. Furthermore, CMIP6 projected GPP and ET_a at the monthly timescale were used to obtain ET_a under the assumed constant trend in WUE (denoted as GPP-based ET_a) and ET_a constrained by historical ET_a estimates during 2015–2018 (denoted as CMIP6-based ET_a), respectively.

2.4. Data for Validating Historical ET_a Estimates

Measured ET_a data at the daily timescale from 25 flux towers (Table S2 in Supporting Information S1) using the eddy covariance system were used to validate historical ET_a estimates. These data can be accessed from the National Tibetan Plateau Data Center (<https://data.tpc.ac.cn/>), Fluxnet2015 (<https://fluxnet.org/data/fluxnet2015-dataset/>), the China Science Data Website (<http://www.csdata.org/p/>), the Data Shared Service Center of the China National Ecological Science Data Center (<http://www.cnern.org.cn/>), and the Institute of Water Science in Pastoral area of the Ministry of Water Resources. To maintain the consistency of data at these flux sites, the energy balance closure correction was not performed. To show the performance of PM ET_a estimates during the historical period, seven global ET_a products (Table S3 in Supporting Information S1) were used for comparison, including GLEAM 3.5a and 3.5b ET_a (Martens et al., 2017), GLASS ET_a (Liang et al., 2021), PML ET_a (Zhang, Y Q et al., 2016), AVHRR ET_a (Zhang, K et al., 2010), FLUXCOM ET_a (Jung et al., 2019), and BESS ET_a (Jiang & Ryu, 2016).

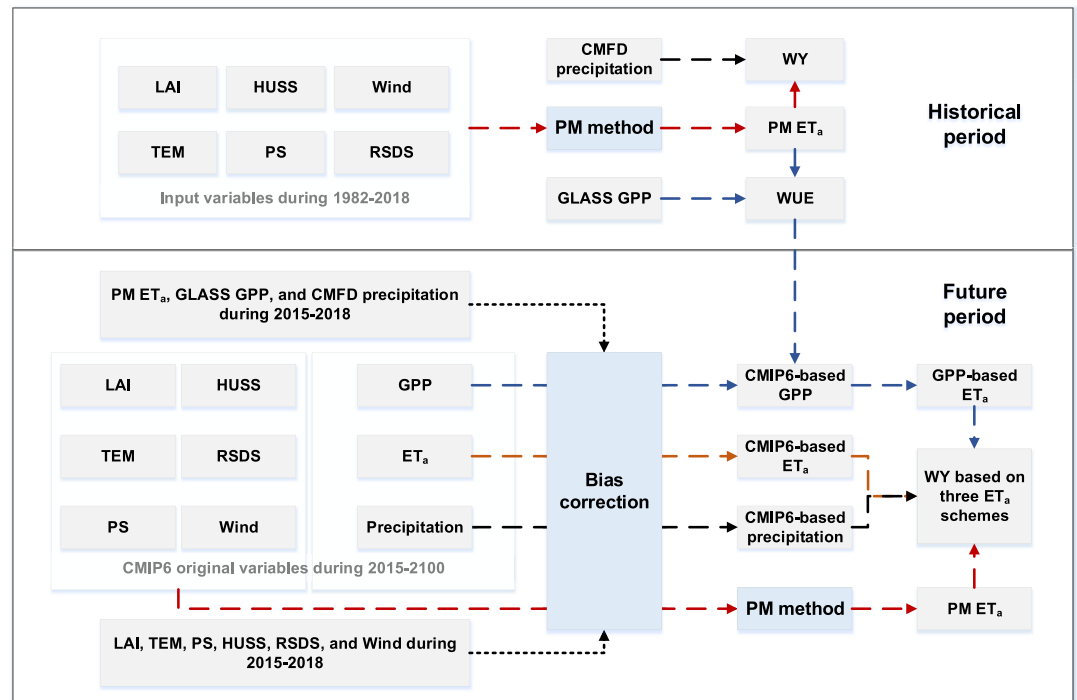


Figure 2. Flowchart of historical estimation and future projection of WY. Rectangles in gray and blue denote data and methods used in this study, respectively. Arrows in red, blue, and orange show calculation processes of PM ET_a , GPP-based ET_a , and CMIP6-based ET_a , respectively. HUSS, Wind, TEM, PS, and RSDS are specific humidity, wind speed, air temperature, surface pressure, and downward solar radiation, respectively.

2.5. Methodology

A flowchart of historical estimation and future projection of ET_a and WY is shown in Figure 2. During 1982–2018, only WY based on diagnostic PM ET_a was generated with CMFD precipitation (Equation 1). To evaluate the impacts of grassland greening on the sustainability of water resources during 2019–2100 considering plant physiological and hydrological feedbacks, three ET_a schemes (PM ET_a , GPP-based ET_a , and CMIP6-based ET_a) were used, in combination with CMIP6-based precipitation. Output from 14 GCMs (Table S1 in Supporting Information S1) that have all input variables of the PM method and ET_a was selected to obtain PM ET_a and CMIP6-based ET_a , whereas output of nine GCMs (Table S1 in Supporting Information S1) that have GPP projections was used to obtain GPP-based ET_a . Projected variables used for the future period in the analysis were all multi-model mean values.

$$WY = P - ET_a \quad (1)$$

where WY is the water yield (mm); P is the precipitation (mm); and ET_a is the evapotranspiration (mm).

2.5.1. Estimation of PM ET_a

The primary equations of the PM framework (Allen et al., 1998) are shown below (Equation 2–12).

$$\lambda ET_a = \frac{\Delta(R_n - G) + \frac{\rho_c V_{PD}}{R_A}}{\Delta + \gamma \left(1 + \frac{R_c}{R_A}\right)} \quad (2)$$

$$R_c = \frac{R_{st}}{LAI \times \text{leaf}_{\text{type}}} \quad (3)$$

where λ is the latent heat of vapourization ($J \cdot kg^{-1}$), with the default value of 2.45; Δ is the slope of saturated vapor pressure and temperature curve ($mb \cdot K^{-1}$); R_n is the net radiation ($W \cdot m^{-2}$); G is the soil heat flux ($W \cdot m^{-2}$); ρ is the

air density (kg m^{-3}); c_p is the heat capacity of moist air at constant pressure ($\text{J kg}^{-1} \text{K}^{-1}$); V_{PD} is the vapor pressure deficit (mb); R_A is the aerodynamic resistance of heat transfer (s m^{-1}); γ is the psychrometric constant (mb K^{-1}); R_c is the canopy stomatal resistance (s m^{-1}), calculated with Equation 3; R_{st} is the minimum (non-stressed) stomatal resistance of a single leaf, with the default value of 167; LAI is the leaf area index ($\text{m}^2 \text{m}^{-2}$); $\text{leaf}_{\text{type}}$ is the stomatal leaf that is bilaterally (i.e., $\text{leaf}_{\text{type}}$ set to 2) or unilaterally (i.e., $\text{leaf}_{\text{type}}$ set to 1), default as unilaterally.

A modification was made in the calculation of aerodynamic roughness length for heat transport (z_{OH}) which is used to obtain the aerodynamic resistance of heat transfer (R_A). The adjustment parameter (kB) that reflects the difference in resistance between heat and momentum transfer (z_{OM} , in Equation 4) was an important parameter for one-source energy balance models (e.g., PM). The value of kB was found to decrease with increases in LAI (Lhomme et al., 2000) and its maximum value could be up to 11.1 (Kustas, W. P. et al., 1989). Therefore, we used Equations 5 and 6 to compute kB instead of the original default value of zero.

$$z_{\text{OH}} = \frac{z_{\text{OM}}}{e^{kB}} \quad (4)$$

$$kB = (1 - f_c) \times 12 \quad (5)$$

$$f_c = 1 - e^{(-0.5 \times \text{LAI} \times \Omega)} \quad (6)$$

where z_{OH} and z_{OM} are the aerodynamic roughness length for heat and momentum transport (m), respectively; kB is the adjustment parameter (-); f_c is the fraction of vegetation cover (-), and its calculation is based on published work (Zhang, C et al., 2021); and Ω is the clumping factor for vegetation (-), with a default value of 0.83 for grassland.

The method to calculate net radiation (R_n , Equations 7–11) originates from the two-source energy balance model (Kustas & Norman, 1999), with the fraction of vegetation greenness (f_g) used to calculate the leaf absorptivity of visible and near-infrared band (Zhang, C et al., 2021) simplified as Equation 9.

$$R_n = R_{n,s} + R_{n,l} \quad (7)$$

$$R_{n,s} = S_{n,c} + S_{n,s} \quad (8)$$

$$f_g = 0.95 \times f_c \quad (9)$$

$$R_{n,l} = emis \times (L_d - \sigma T_{\text{atm}}^4) \quad (10)$$

$$L_d = emis_{\text{atm}} \times \sigma \times (T_{\text{atm}} - \text{lapse} \times z_T)^4 \quad (11)$$

where $R_{n,s}$ and $R_{n,l}$ are the net shortwave and net longwave radiation (W m^{-2}); $S_{n,c}$ and $S_{n,s}$ are the net shortwave radiation for canopy and soil (W m^{-2}); $emis$ is the surface emissivity (-), with a default value of 0.95; L_d is the downward longwave radiation (W m^{-2}); σ is the Stephan Boltzmann constant of $5.67e^{-8} \text{W m}^{-2} \text{K}^{-4}$; T_{atm} is the air temperature (K); $emis_{\text{atm}}$ is the effective atmospheric emissivity (-); lapse is the moist-adiabatic lapse rate (K m^{-1}); and z_T is the air temperature measurement height, with a default value of 2 m.

The method to calculate the soil heat flux (G) is shown in Equation 12. The commonly used method to calculate G shows significant overestimation and cannot reflect the negative value of G during the non-growth period of grass (Gu et al., 2005; Purdy et al., 2016), including periods of January–April and October–December. G is higher during the grass growth period from April to August, consistent with variations in f_c . Therefore, Equation 12 was used in this study. The ratio of 0.16 in Equation 12 was obtained by the commonly used default ratio of 0.31 (Purdy et al., 2016) multiplied by 0.5, and the value of -0.06 was referred to as the average ratio of G to R_n measurements during the post-growth period of grass (Gu et al., 2005).

$$G = R_n \times (0.16 \times f_c - 0.06) \quad (12)$$

2.5.2. Estimation of GPP-Based ET_a

The trend in annual WUE during 1982–2018 was kept constant, and GPP-based ET_a at the annual timescale was obtained using CMIP6 GPP_{corr} (bias-corrected CMIP6 GPP) and projected WUE in the respective year during 2019–2100 (Equations 13 and 14). The regression between historical WUE and year number was performed for

each pixel, after the historical WUE during 1982–2018 was aggregated to match the spatial resolution of CMIP6 projections ($\sim 0.94^\circ$).

$$WUE_y = a + b \times y \quad (13)$$

$$ET_{a,GPP\text{-based},y} = GPP_{CMIP6,corr,y} \div WUE_y \quad (14)$$

where WUE_y is the water use efficiency for the y year during 2019–2100; a and b are the fitted intercept and slope using historical WUE and year number during 1982–2018, respectively; and $ET_{a,GPP\text{-based},y}$ and $GPP_{CMIP6,corr,y}$ are the annual GPP-based ET_a and CMIP6 GPP_{corr} for the y year during 2019–2100.

2.5.3. Correction for CMIP6 Projections

Three bias correction methods were used to correct different variables, including the delta approach, ratio method, and quantile mapping (Gudmundsson et al., 2012; Wood et al., 2004). The CMIP6 climatic forcing data including air temperature, surface pressure, and downward solar radiation during 2019–2100 were corrected using the delta approach, as shown in Equation 15. These CMIP6 data for the separate months were corrected using the average bias of spatially averaged values for grassland pixels between historical data and CMIP6 data for the corresponding month during overlapping periods (i.e., 2015–2018). For CMIP6 projections of LAI, specific humidity, wind speed, ET_a , and GPP data, the ratio method was used (i.e., Equation 16). CMIP6 projected precipitation was corrected using the cumulative distribution function matching-based quantile mapping (Equations 17 and 18). Equation 18 is used to map the raw CMIP6 variable to the same distribution as the historical variable. Namely, raw CMIP6 precipitation for a given month was multiplied by the ratio of corrected spatially averaged CMIP6 precipitation for grassland pixels and the original one for the corresponding month.

Results (Figures S1 and S2 in Supporting Information S1) show that temporal variations in monthly corrected CMIP6 variables during 2015–2018 are consistent with variations of historical data, indicating the suitability of the bias correction methods for different variables. To further reduce errors that still exist after bias correction (Figure S2 in Supporting Information S1), we deducted the deviation between the corresponding spatially averaged values of projected WY and historical WY in 2018, when obtaining the spatially averaged WY and the spatial pattern of WY for NCTP and the three sub-regions.

$$X'_{c,y,i} = X'_{o,y,i} - \frac{\sum_{hy=2015}^{2018} (X_{o,hy,i} - X_{h,hy,i})}{4} \quad (15)$$

$$X'_{c,y,i} = X'_{o,y,i} \div \frac{\sum_{hy=2015}^{2018} (X_{o,hy,i} \div X_{h,hy,i})}{4} \quad (16)$$

$$X_{c,y,i} = F_{h,i}^{-1}(F_{o,i}(X_{o,y,i})) \quad (17)$$

$$X'_{c,y,i} = \frac{X_{c,y,i}}{X_{o,y,i}} \times X'_{o,y,i} \quad (18)$$

where $X'_{c,y,i}$ and $X'_{o,y,i}$ are the corrected and original CMIP6 data for month i in y year, respectively; subscript y ranges from 2019 to 2100; $X_{o,hy,i}$ and $X_{h,hy,i}$ are the area-weighted spatial averages for all grassland pixels from original CMIP6 data and historical data for month i in hy year, respectively; subscript hy is the overlap years (2015–2018) between historical data and CMIP6 data; $F_{o,i}$ is the cumulative distribution function (CDF) of original area-weighted spatial averages for all grassland pixels from CMIP6 data for month i (i.e., $X_{o,y,i}$ for y ranging from 2019 to 2100); $F_{h,i}^{-1}$ is the inverse CDF corresponding to area-weighted spatial averages for all grassland pixels from historical data for month i (i.e., $X_{h,hy,i}$ for hy ranging from 2015 to 2018); and $X_{c,y,i}$ is the corrected area-weighted spatial averages of all grassland pixels from CMIP6 data for month i for y ranging from 2019 to 2100.

2.5.4. Projection of Herbivore Stocking Numbers

Based on CMIP6 data, stocking numbers of herbivores (i.e., sheep and cattle) during 2019–2100 in four major provinces/autonomous regions (i.e., Inner Mongolia, Qinghai, Tibet, and Xinjiang) of NCTP were projected from

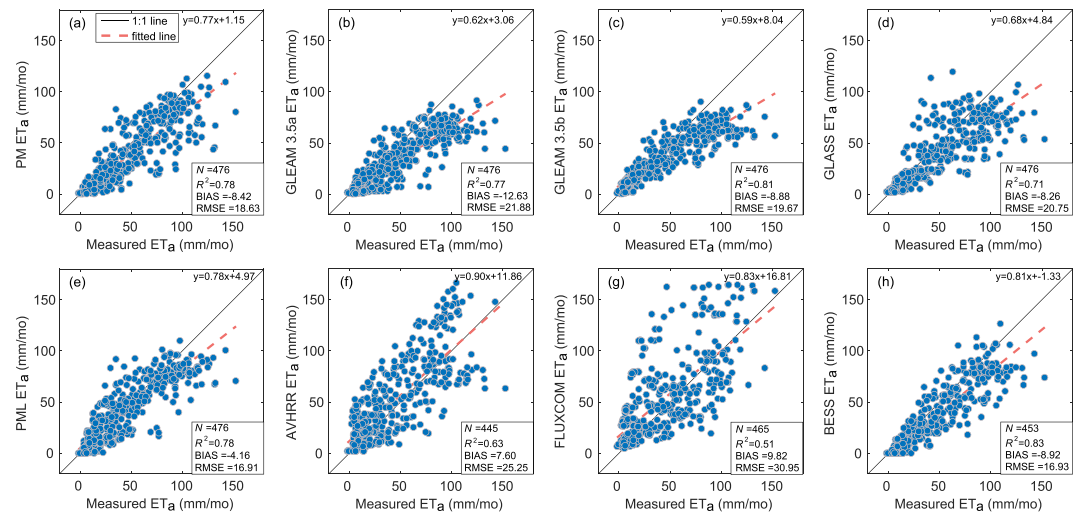


Figure 3. Scatterplots of PM ET_a (a) and seven global ET_a datasets (i.e., GLEAM 3.5a ET_a (b), GLEAM 3.5b ET_a (c), GLASS ET_a (d), PML ET_a (e), AVHRR ET_a (f), FLUXCOM ET_a (g), and BESS ET_a (h)) against measured ET_a for 14 flux stations at the monthly timescale, as well as the respective statistical metrics and regression of fitted lines.

CMIP6 variables, using multiple linear regression on historical data (Equation 19). Reported stocking numbers of herbivores during the historical period were obtained from provincial statistical yearbooks. Validation results (Figure S3 in Supporting Information S1) show the appropriateness of multiple linear regression to estimate herbivore stocking numbers for different provinces/autonomous regions, with a coefficient of determination (R^2) of modeled stocking numbers of herbivores against reported numbers of 0.82. For the future projection, the area-weighted spatial average of CMIP6 LAI_{corr} (bias-corrected CMIP6 LAI), CMIP6-based ET_a, CMIP6-based precipitation, and CMIP6 TEM_{corr} (bias-corrected CMIP6 air temperature) were used. Lastly, when obtaining the final projected stocking numbers of herbivores for respective provinces/autonomous regions during 2019–2100, the corresponding deviation between modeled and reported numbers in 2019 was deducted.

$$\text{Herbivore}_{\text{number}} = a_1 + b_1 \times \text{LAI} + b_2 \times \text{ET}_a + b_3 \times P + b_4 \times T_{\text{atm}} \quad (19)$$

where a_1 , b_1 , b_2 , b_3 , and b_4 are fitted parameters.

3. Results

3.1. Validation of ET_a Estimates With the Diagnostic PM Method

The diagnostic PM approach was used to project ET_a for comparison with prognostic ET_a results during the future period; therefore, accurately estimating ET_a during the historical period is crucial. To verify the accuracy of ET_a estimation with the PM framework, measured ET_a data (Table S2 in Supporting Information S1) at 25 flux stations under grassland shown in Figure 1 were used for validation at daily and monthly timescales during the historical period. Seven other global ET_a datasets were used for comparison (Table S3 in Supporting Information S1). Based on statistical metrics against measured ET_a (Figure S4 in Supporting Information S1), PM ET_a at the daily timescale shows higher accuracy than GLEAM 3.5a ET_a (Martens et al., 2017). Performance of PM ET_a at the monthly timescale was comparable with that of three global ET_a datasets (GLEAM 3.5b ET_a (Martens et al., 2017), PML ET_a (Zhang, Y Q et al., 2016), and BESS ET_a (Jiang & Ryu, 2016)), and outperformed performance of the other four ET_a datasets (Figure 3).

Temporal variations in WY across NCTP during the historical period were examined using PM ET_a and five other ET_a products (GLEAM3.5a ET_a, GLASS ET_a (Liang et al., 2021), PML ET_a, FLUXCOM ET_a (Jung et al., 2019), and BESS ET_a), chosen for their timespan and performance (Figures 4a–4d). Precipitation from the CMFD (He et al., 2020) was used to reflect changes in water supply, given its better performance across NCTP than the other three global precipitation datasets (Figure S5 in Supporting Information S1). Results show that interannual variations in WY based on PM ET_a and the other four ET_a datasets are consistent in NCTP (Figure 4a), except for

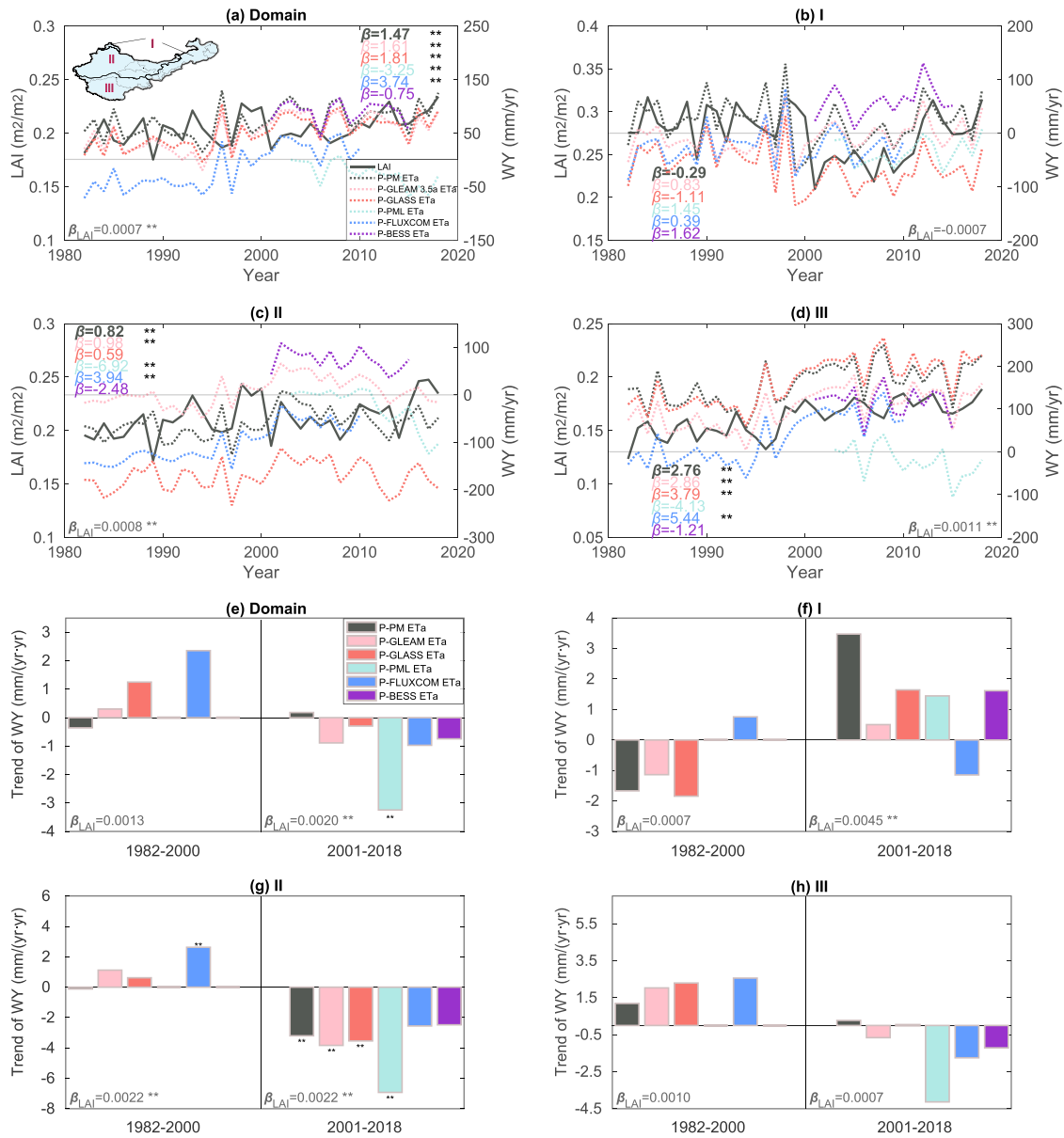


Figure 4. Temporal variations (a–d) and trends (e–h) in the annual leaf area index (LAI) and annual water yield (i.e., WY, calculated from the CMFD precipitation dataset and PM ET_a and the other five ET_a products) for NCTP and three sub-regions during 1982–2018. The insert in the upper left corner of subplot a shows the boundaries of NCTP and three sub-regions. In subplots a–d, linear trends fitted to the six WY datasets (i.e., the β coefficients) and annual LAI (i.e., β_{LAI}) are shown and marked with “***” (with the Mann-Kendall test at a 5% significance level). In subplots e–h, bars are trends in annual WY calculated using PM ET_a, GLEAM 3.5a ET_a, GLASS ET_a, PML ET_a, FLUXCOM ET_a, and BESS ET_a. Fitted linear trends in annual LAI (i.e., β_{LAI} , in the lower left of each plot) and annual WY (i.e., values represented by bars) for two periods during 1982–2000 and 2001–2018 were marked with “***” (with the Mann-Kendall test at a 5% significance level) in subplots e–h.

the WY based on PML ET_a (due to the inconsistency in region III). As for the three sub-regions (Figure 4b–4d), among the five ET_a products, the magnitude and trend of WY based on PM ET_a is consistent with that of WY based on GLEAM3.5a ET_a. These results indicate the suitability of PM ET_a for the analysis of historical WY as well as for projected WY. If not stated otherwise, the following analysis during the historical period used PM ET_a-based WY.

3.2. Analysis of Water Yield During the Historical Period

Annual WY in NCTP is always positive during 1982–2018 (Figure 4a), whereas WY for the three sub-regions shows different characteristics over the past four decades, implying the probably diversified outcomes of their

WY in the future. Grass growth in region II appears to be continuously depleting regional water storage, because annual WY is consistently below zero (Figure 4c). Grass growth in region III is not constrained by water supply with annual WY always greater than zero (Figure 4d), whereas annual WY in region I fluctuates around zero (Figure 4b). Meanwhile, temporal variations in annual WY were ahead of those in LAI for regions I and III for 1–2 years with their correlation coefficients ranging from 0.45 to 0.73, whereas this is not the case for region II. This suggests that grass growth in region II is not as dependent on precipitation as in regions I and III, but relies more on glacier and snow meltwater (Chen, Y et al., 2015; Luo et al., 2018).

Ecological restoration programs have driven strong vegetation growth since the early 2000s, with a negative effect of increased vegetation cover on water resources (Zhao, M et al., 2021). Here, for the period during 1982–2018, we find that annual WY across the entire NCTP region increased synchronously with annual LAI, particularly for regions II and III (Figure 4c–4d). Nevertheless, trends in annual WY during 2001–2018 based on the six ET_a products across NCTP and three sub-regions are generally opposite to the trends observed during 1982–2000 (Figure 4e–4h). Annual WY based on the six ET_a products in regions II and III showed a decreasing trend during 2001–2018 while annual LAI continued to increase. This indicates that grassland greening may have a negative impact on regional water resources during the historical period, particularly for region II without sufficient precipitation to meet the water consumption of grassland.

Spatial patterns of mean annual WY based on PM ET_a and LAI during 1982–2000 and 2001–2018 were examined as well as the difference of each variable between the two periods. There is no obvious correspondence between the spatial patterns in mean annual WY and LAI (Figure 5), indicating that grass growth is also constrained by other factors (e.g., air temperatures in high mountain areas of region III (Zhao, W et al., 2020)). Temporal changes in mean annual WY respond to changes in LAI (Figures 5c and 5f), because areas with opposite signs of ΔLAI and ΔWY (i.e., $\Delta LAI \geq 0$ and $\Delta WY < 0$; $\Delta LAI < 0$ and $\Delta WY \geq 0$) between two periods accounted for ~62% of grassland in NCTP (Figure 5h). Note that Δ denotes the value during 2001–2018 minus the value during 1982–2000. Areas with positive ΔLAI and negative ΔWY accounting for 27% of grassland across NCTP, are primarily located in the south of NCTP ranging from 85°E to 115°E. Potential negative impacts of grassland greening on regional water resources in these regions require more attention. More positively, 64% of grassland in NCTP had higher WY during 2001–2018 than 1982–2000, although 56% of grassland in NCTP had higher LAI during 2001–2018 than 1982–2000 (Figure 5h). Areas with positive ΔLAI and ΔWY accounted for ~29% of grassland in NCTP, located mostly in region III. Therefore, the complex effects of grassland greening, climate change, and hydrological and plant physiological feedbacks to climate change on future regional water resource sustainability need to be clarified (see the following sections).

3.3. Future Water Yield Under Climate Change

We explored the interplay between vegetation greening and water resource sustainability (which depends on changes in WUE and evaporation recycling alongside greening) using three ET_a schemes in future projections. The diagnostic PM ET_a scheme was utilized as a connection between the historical and future periods, driven directly by atmospheric water demand and vegetation greening. The prognostic GPP-based ET_a scheme (based on CMIP6-based GPP and projected WUE (keeping its trend consistent with the history)) revealed a persistent influence of the relatively rapid increasing WUE on WY. The CMIP6-based ET_a scheme (based on bias-corrected CMIP6 ET_a) represents the ensemble WY of prognostic models, considering the combined influence of WUE and evaporation recycling.

According to CMIP6 projections, the greening of grassland across NCTP is expected to continue during 2019–2100 (Figure 6). Overall, for the three CMIP6 scenarios (i.e., SSP126, SSP245, and SSP585), increasing trends in annual CMIP6 LAI_{corr} (bias-corrected CMIP6 LAI) across NCTP during 2019–2100 are 3×10^{-4} , 6×10^{-4} , and $1.3 \times 10^{-3} \text{ m}^2/(\text{m}^2\cdot\text{yr})$, respectively. These trends are lower than the increasing trend in annual LAI ($2 \times 10^{-3} \text{ m}^2/(\text{m}^2\cdot\text{yr})$) during 2001–2018, indicating the slowdown of grassland greening in the future. Meanwhile, annual WY based on three ET_a schemes shows a simultaneously increasing trend with LAI and is always positive for all three scenarios. In particular, the increasing trend in annual WY based on GPP-based ET_a is greater than the trend based on CMIP6-based ET_a , and the lowest increasing trend is found in annual WY based on PM ET_a . This indicates that annual WY based on diagnostic PM ET_a can be considered the least sustainable scheme for regional water resources. In addition, increasing trends in annual WY based on the three ET_a schemes are larger under the higher emissions scenario, corresponding to changes in trends of CMIP6 LAI_{corr} . This is because the increase in

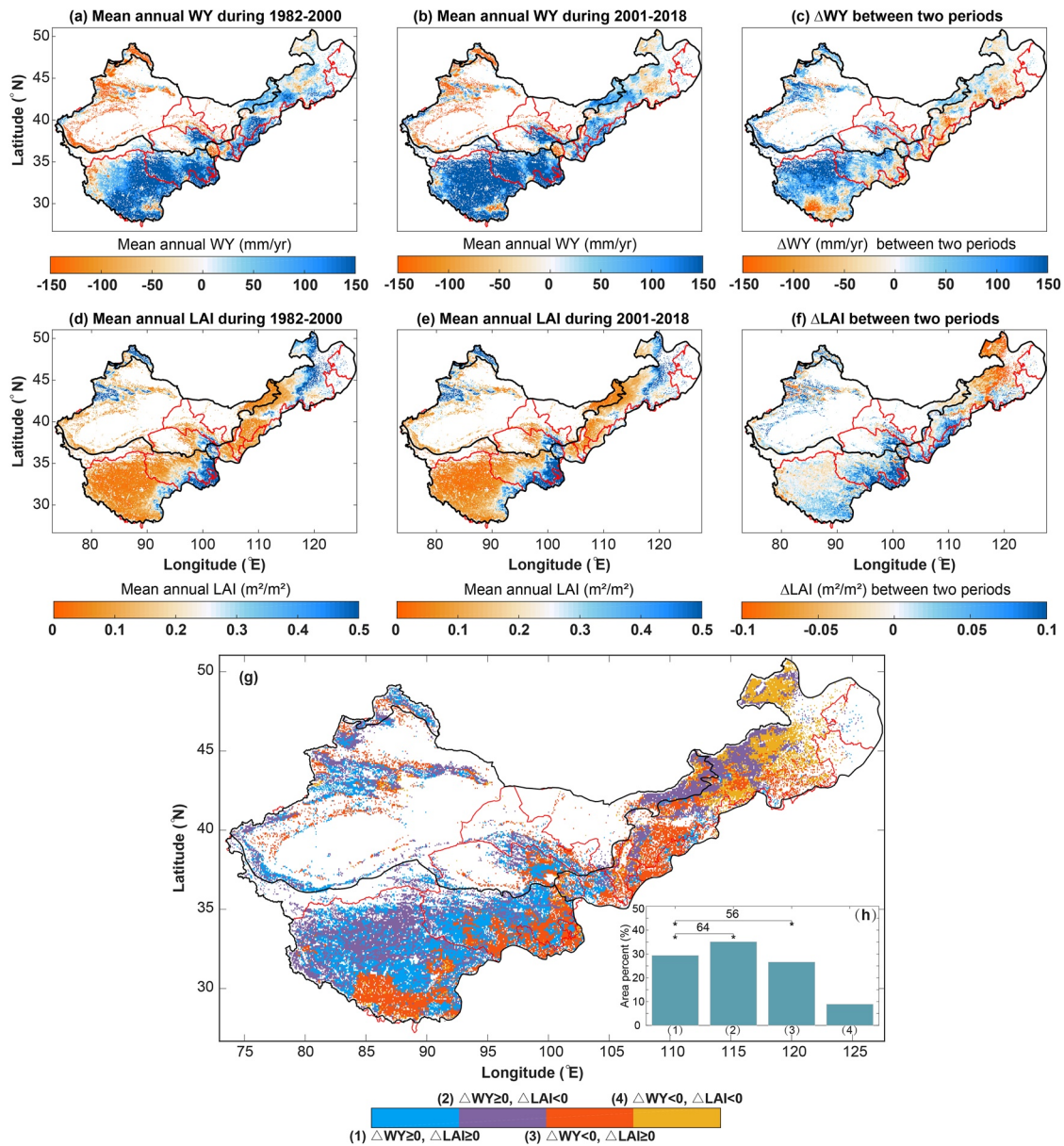


Figure 5. Spatial patterns in mean annual WY and LAI are shown for the periods 1982–2000 (a and d) and 2001–2018 (b and e), along with the difference in mean annual WY and LAI between the two periods (c and f, i.e., the later minus the earlier period). Spatial patterns (g) and respective area percentages (h) for four categories of the difference in mean annual WY and LAI between periods of 1982–2000 and 2001–2018 (i.e., (1) $\Delta WY \geq 0$ and $\Delta LAI \geq 0$, (2) $\Delta WY \geq 0$ and $\Delta LAI < 0$, (3) $\Delta WY < 0$ and $\Delta LAI \geq 0$, and (4) $\Delta WY < 0$ and $\Delta LAI < 0$). ΔWY (ΔLAI) is the mean annual WY (mean annual LAI) during 2001–2018 minus the mean annual WY (mean annual LAI) during 1982–2000.

precipitation exceeds the increase in ET_a as carbon emissions increase. These findings suggest that both grassland greening and increased regional water resources may coexist in the future based on the climate projections.

Among the three sub-regions (Figures S6–S8 in Supporting Information S1), upward trends in annual CMIP6 LAI_{corr} during 2019–2100 for regions I and III under the three scenarios are close to the trends estimated for the entire NCTP region, whereas the upward trends in annual CMIP6 LAI_{corr} in region II are the lowest. Correspondingly, the projected annual WY based on the three ET_a schemes in regions I and III is always positive, whereas there are significant discrepancies in annual WY of region II under different ET_a schemes. Compared with the historical period (Figure 4b), the water resource sustainability of region I has notable improvement. However, the WY based on three ET_a estimates for region II differs greatly. Only annual WY using GPP-based ET_a and CMIP6-based ET_a exhibits continued increases and shifts from negative to positive under the three scenarios. As

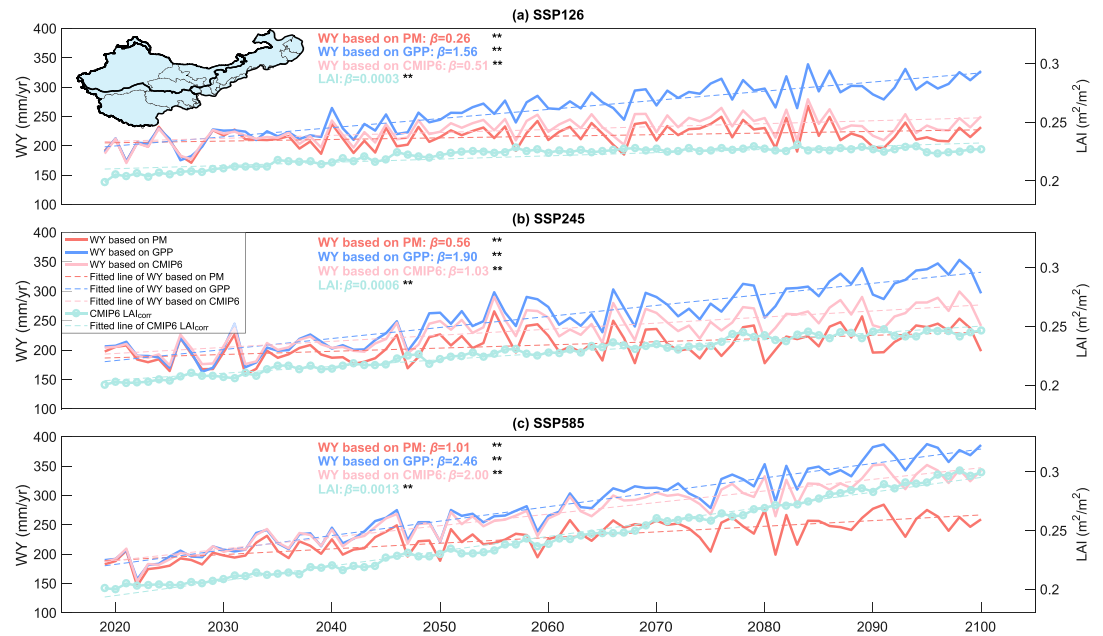


Figure 6. Temporal variations in CMIP6 multi-model ensemble mean WY (based on PM ET_a , GPP-based ET_a , and CMIP6-based ET_a) and LAI_{corr} across NCTP during 2019–2100 under SSP126 (a), SSP245 (b), SSP585 (c) scenarios, as well as respective fitted linear trends marked with “**” (with the Mann-Kendall test at a 5% significance level). The insert in the upper left corner of subplot a shows the boundaries of NCTP and the three sub-regions.

for the PM ET_a scheme, only annual WY under the SSP126 scenario fluctuates around zero, with its magnitude and trend greater than those under the SSP245 and SSP585 scenarios. This indicates that grass growth in region II is expected to continue to consume water storage (e.g., glacier meltwater and groundwater) in the future, most likely exacerbating the water crisis.

3.4. Spatial Variability in Future Projections of Water Yield

In future projections, mean annual CMIP6 LAI_{corr} shows an increasing trend in almost the entire NCTP region during 2019–2100, along with the growth in carbon emissions (Figure 7). Unexpectedly, overall areas with negative mean annual WY (i.e., $WY < 0$) are likely to reduce (Figure 7) against those during the historical period (Figure 5). Meanwhile, regions with simultaneously increased LAI and WY dominated NCTP during the future period (Figure 8), accounting for more than 50% of NCTP grassland (much larger than 29% in Figure 5 during the historical period). Nevertheless, other regions with high potential for water insecurity may emerge in the future. Negative mean annual WY based on PM ET_a and CMIP6-based ET_a is shown in the same areas of region II (e.g., Tian Shan, Qilian Shan, and the border of Ningxia and Inner Mongolia). Mean annual WY based on CMIP6-based ET_a also shows significantly negative values in northern Tibet and central Qinghai, whereas there are scattered areas in central parts of Inner Mongolia, Tibet, and Xinjiang autonomous regions with negative mean annual WY based on GPP-based ET_a .

In general, continuous increases in CMIP6 LAI_{corr} affect water resource availability in parts of regions I and III, but may have a larger impact in region II. During the historical period, global warming accelerates glacier melting in high mountain regions of China (e.g., the Kunlun Mountains and Tian Shan in region II) (Brun et al., 2017; Hugonnet et al., 2021), promoting vegetation greening with increased soil moisture (Maina et al., 2022). Nevertheless, without positive WY providing sufficient supply, the continued greening of grassland is expected to consume regional water resources, becoming unsustainable in the future.

Meanwhile, periods in which increased LAI may affect water resource availability also deserve attention, though the increasing trend in CMIP6 LAI_{corr} in some regions of NCTP is likely to turn into a decreasing trend over the future period, particularly for the SSP126 scenario (Figure S9 in Supporting Information S1). Therefore, the future period was divided into three sub-periods, 2019–2050, 2051–2080, and 2081–2100, to further investigate

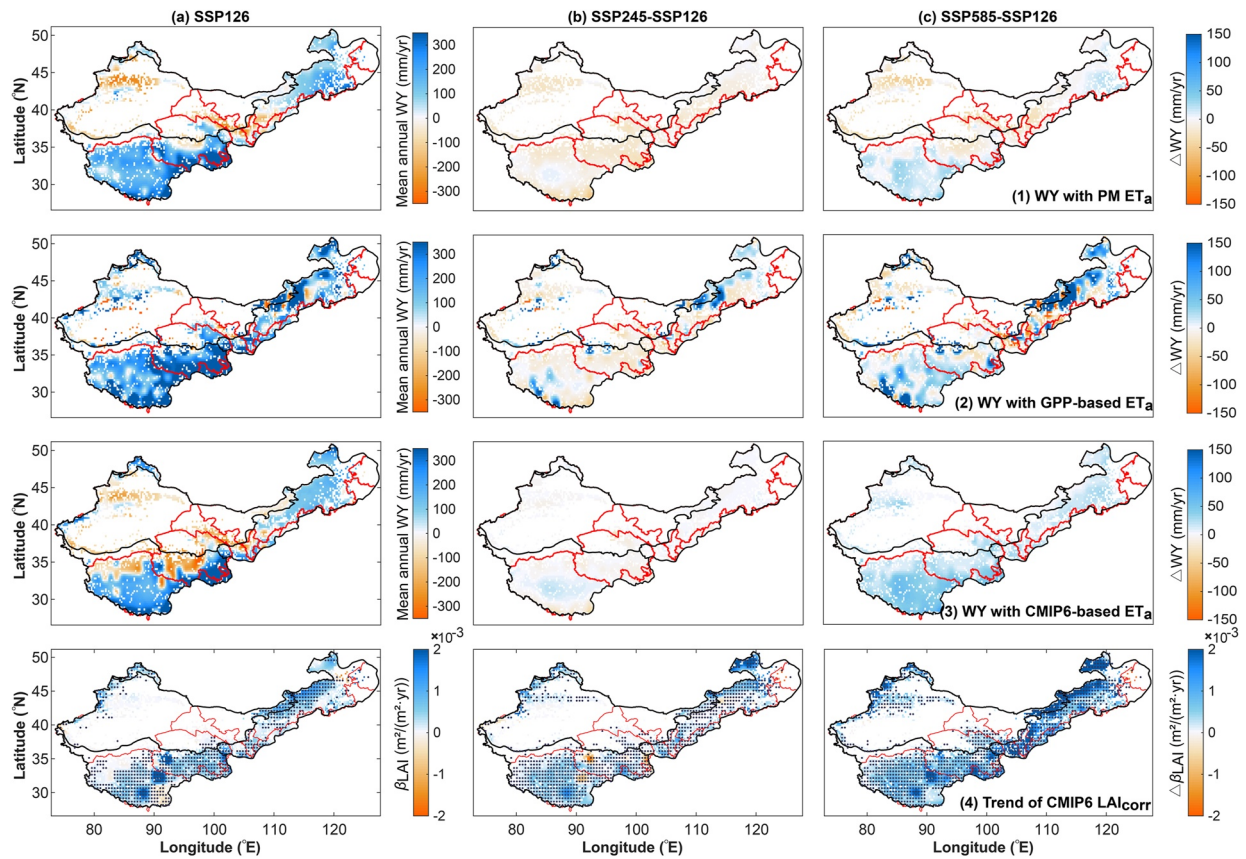


Figure 7. Spatial patterns in mean annual WY based on PM ET_a (row 1), GPP-based ET_a (row 2), and CMIP6-based ET_a (row 3) and trend in annual CMIP6 LAI_{corr} (row 4) during 2019–2100 under SSP126 (column a), as well as the difference in mean annual WY and trend in annual CMIP6 LAI_{corr} between the SSP245 and SSP126 scenarios (column b) and between the SSP585 and SSP126 scenarios (column c). The trend in annual CMIP6 LAI_{corr} is denoted as β_{LAI} and the difference between two scenarios is denoted as Δ . Stippling in the last row of the graph indicates regions where the trend in annual CMIP6 LAI_{corr} for respective scenarios is statistically significant (with the Mann-Kendall test at a 5% significance level).

the connection between trends in annual WY and annual LAI (i.e., β_{WY} and β_{LAI}) over time. In general, only in the SSP585 scenario, areas with simultaneous increases in both WY and LAI are dominant (>68%) for all three ET_a schemes and in all three sub-periods (see the third row in Figure 8 and Figures S10–S11 in Supporting Information S1). Under the SSP126 scenario (see the first row in Figure 8 and Figures S10–S11 in Supporting Information S1), in contrast, areas with decreased WY are widespread during the late 21st century (2081–2100), though areas with increased WY are dominant (>73%) before then (during 2019–2080). More areas show decreases in both WY and LAI during 2081–2100 under the SSP126 scenario.

For the SSP245 scenario, spatial patterns in four categories of β_{WY} and β_{LAI} (i.e., (a) $\beta_{WY} \geq 0$ and $\beta_{LAI} \geq 0$, (b) $\beta_{WY} \geq 0$ and $\beta_{LAI} < 0$, (c) $\beta_{WY} < 0$ and $\beta_{LAI} \geq 0$, and (d) $\beta_{WY} < 0$ and $\beta_{LAI} < 0$) are different for the three ET_a schemes. Based on PM ET_a and CMIP6-based ET_a , the proportion of areas with decreased WY and increased LAI is largest during 2051–2080 with area percentages up to 74% and 56%, respectively (see the second row in Figure 8 and Figure S11 in Supporting Information S1). Based on GPP-based ET_a , areas with both increases in WY and LAI are dominant (>51%) for all three sub-periods under the SSP245 scenario (see the second row in Figure S10 in Supporting Information S1). Overall, the SSP585 scenario shows the most positive results with both grassland and regional water resources, whereas 2081–2100 (2051–2080) is the period of concern for the SSP126 (SSP245) scenario.

3.5. Effects of Grassland Greening, Increased Water Use Efficiency, and Intensified Evaporation Recycling on ET_a and Water Yield

Figure 9 shows a schematic diagram of the multifaceted effects of grassland greening, climate change (e.g., increased atmospheric water transport, elevated CO_2 , and climate warming), and intensified evaporation recycling

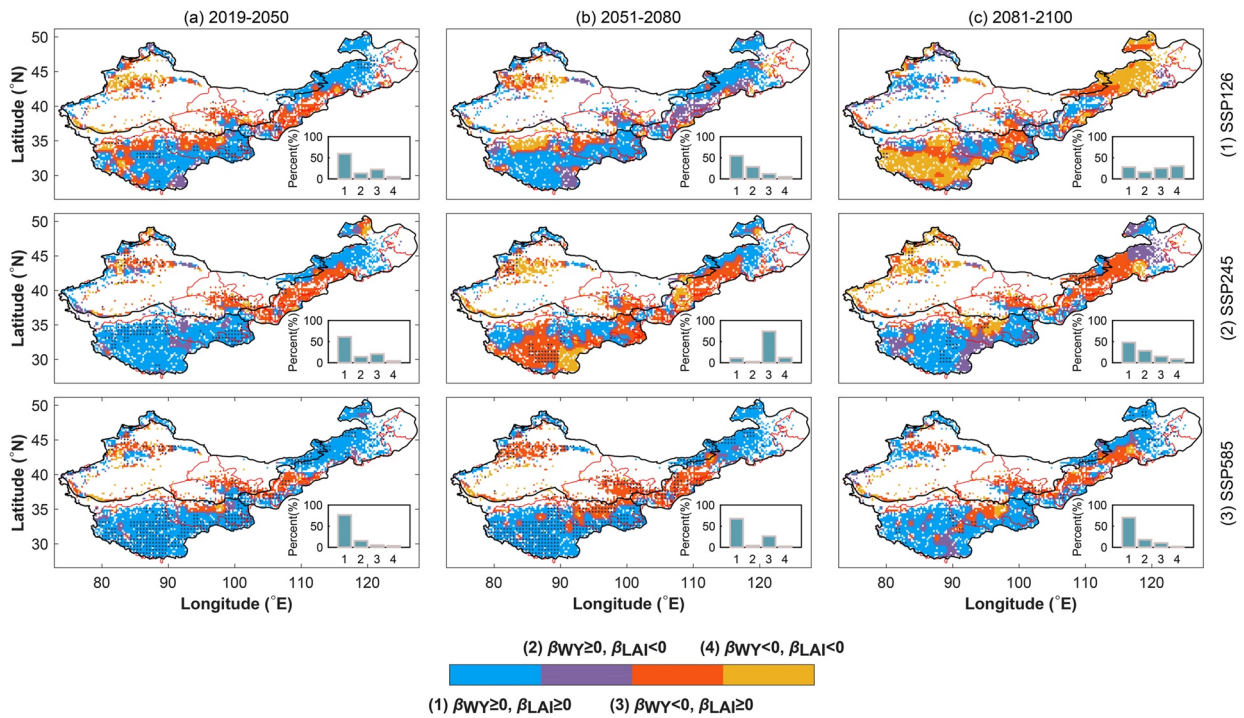


Figure 8. Spatial patterns and respective area percentages for four categories (i.e., (1) $\beta_{WY} \geq 0$ and $\beta_{LAI} \geq 0$, (2) $\beta_{WY} \geq 0$ and $\beta_{LAI} < 0$, (3) $\beta_{WY} < 0$ and $\beta_{LAI} \geq 0$, and (4) $\beta_{WY} < 0$ and $\beta_{LAI} < 0$) of trends in annual WY based on PM ET_a and annual LAI during 2019–2050 (column a), 2051–2080 (column b), and 2081–2100 (column c) under the SSP126 (row 1), SSP245 (row 2), and SSP585 scenarios (row 3). Note that trends in annual WY and annual LAI are denoted as β_{WY} and β_{LAI} , respectively. Stippling indicates regions where both the trends in annual WY and CMIP6 LAI_{corr} are statistically significant with the Mann-Kendall test at a 5% significance level.

on WY from a perspective of precipitation and ET_a . Future projections of climate change suggest an increase in atmospheric water transport over NCTP (Fan et al., 2021; Li, Y et al., 2019). Meanwhile, the large-scale vegetation restoration projects are likely to intensify intraregional water recycling processes, thereby increasing precipitation (Wang, X et al., 2021). In our study, even under the most negative scheme with PM ET_a , the coexistence of increased WY and LAI is likely to prevail and WY is always positive for most regions of NCTP. Therefore, increased precipitation caused by atmospheric water transport and evaporation recycling is sufficient to meet the increased water consumption of large-scale grassland greening (Figure S12 in Supporting Information S1).

Three aspects are competing to influence changes in ET_a , including increased WUE, intensified evaporation recycling, and vegetation greening. These three factors can be understood from a perspective of plant physiological (Figure 9a) and hydrological feedbacks (Figure 9b). Plant physiological feedbacks (Witte et al., 2006) include the temperature effect (when plants consume more water to regulate leaf temperature, leading to an increase in ET_a), the LAI effect (when plants produce more biomass with elevated CO_2 , leading to an increase in LAI and also ET_a), and the WUE effect (when plants can meet C-requirements more easily with elevated CO_2 , leading to a decrease in stomatal conductance and ET_a). Hydrological feedback includes evaporation recycling intensified by grassland greening.

In this study, three ET_a schemes were used to quantify the influence of these factors on ET_a . The comparison between CMIP6-based ET_a and GPP-based ET_a helps understand the effect of increased WUE on ET_a , because the difference in ET_a estimates between the two schemes primarily lies in different increasing trends in WUE (β_{WUE}). An increase in WUE is found to result in a decrease in ET_a , with the decreased ratio up to 12% between these two schemes under the SSP126 scenario (Figure 9c). With the increase in carbon emissions, the difference in β_{WUE} between CMIP6-based ET_a and GPP-based ET_a gradually decreases, so the effect of increasing WUE on the decrease in ET_a gradually weakens. On the other hand, by assuming that future WUE maintains the same historical WUE growth trend, the GPP-based ET_a scheme shows the maximum potential impact of WUE on ET_a . The CMIP6-based ET_a scheme shows the final ET_a projection under the combined and projected influence of the temperature, LAI, and WUE effects. Thus, the comparison between these two ET_a schemes reveals plant physiological effects on future ET_a . An increase in ET_a due to the temperature and LAI effects would be larger than a

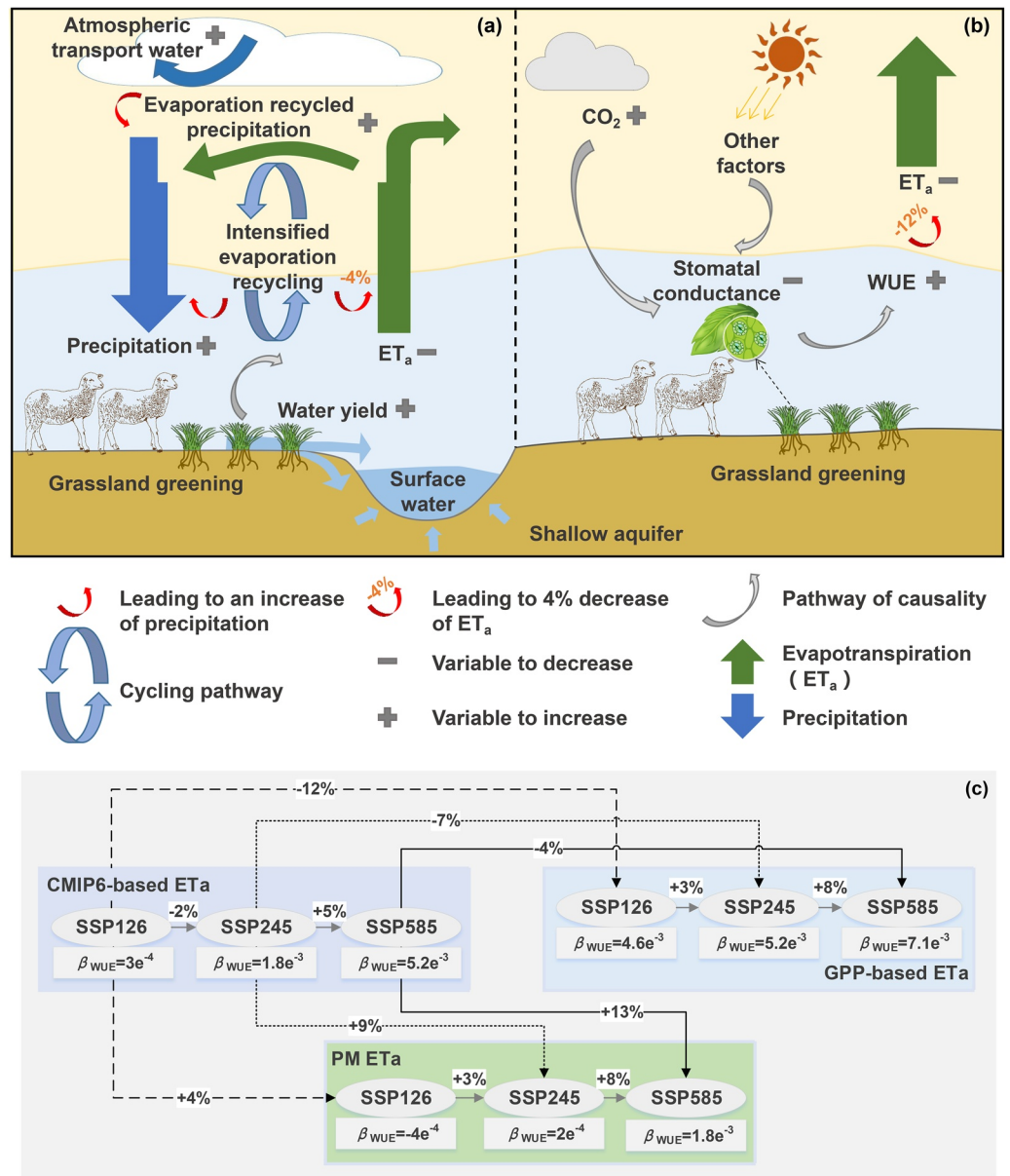


Figure 9. Schematic diagram (a) and (b) illustrating the effects of grassland greening on water yield based on projected precipitation and ET_a in an intensified hydrological cycle with ongoing elevated CO_2 . Estimates in subplots a and b are based on the difference between ET_a schemes under the SSP126 scenario. Subplot c shows differences between multi-year and multi-model ensemble mean ET_a estimates for the three schemes and three scenarios. Percentages shown along the arrows in subplot c are obtained by the equation: $(ET_{a, \text{scenario at point of the arrow}} - ET_{a, \text{scenario at tail of the arrow}}) / ET_{a, \text{scenario at tail of the arrow}}$. β_{WUE} is the trend in annual WUE (calculated using annual CMIP6 GPP_{corr} and respective annual ET_a) during 2019–2100.

decrease in ET_a arising from the WUE effect, because CMIP6-based ET_a increases for all SSP scenarios, while GPP-based ET_a decreases for the SSP126 and SSP245 scenarios (Figure S12 in Supporting Information S1) under the consistent influence of temperature and LAI effects.

In addition, the comparison between CMIP6-based ET_a and PM ET_a shows the combined effects of increased WUE and intensified evaporation recycling on projected ET_a . This is because PM ET_a does not consider the influence of increasing WUE and intensified evaporation recycling, while CMIP6-based ET_a does. Intensified evaporation recycling would also lead to a decrease in ET_a (Figure 9c), because a decrease of 4% in ET_a is found when β_{WUE} for these two schemes (i.e., CMIP6-based ET_a and PM ET_a) is close to zero under the SSP126 scenario (i.e., under the same condition for temperature, LAI, and WUE effects).

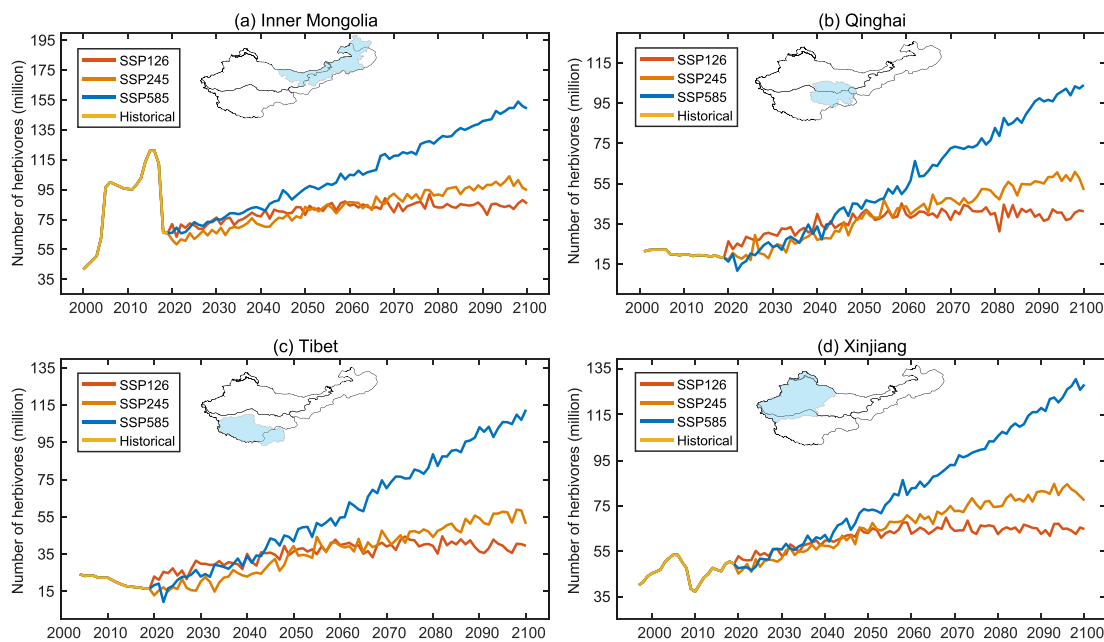


Figure 10. Projections of future herbivore stocking numbers in the four provinces/autonomous regions. Projected stocking numbers of herbivores in Inner Mongolia (a), Qinghai (b), Tibet (c), and Xinjiang (d) provinces/autonomous regions during 2019–2100 under three scenarios, as well as reported numbers during the historical period (1997–2019). The regions highlighted in blue in the NCTP boundary in the top of each panel indicate the geographical location of respective provinces/autonomous regions.

4. Discussion

4.1. Seasonality in Water Yield During the Historical and Future Periods

In the future, projections indicate an increase in the number of months when the water consumption of grass growth (i.e., ET_a) could be met by rainfall in the three sub-regions (Figure S13 in Supporting Information S1) relative to the historical period (Figure S14 in Supporting Information S1). During 1982–2018, the monthly climatology of WY across NCTP was always larger than zero (Figure S14e in Supporting Information S1). There are several periods in the three sub-regions when precipitation may not be sufficient to support water consumption by grassland, including 4 months (May, June, August, and September) in region I, most months in region II, and November in region III. In the future, we find that there are likely to be fewer months with a monthly climatology of WY below zero (Figure S13 in Supporting Information S1). For instance, precipitation in region I may not be sufficient to support water consumption during critical periods of grass heading (i.e., May and June). In region II, grass from June to October may need to rely on other water supplies (e.g., glacier melt). Region III is the most positive area to support the coexistence of increased WY and LAI in the future, with all average monthly WY larger than zero.

4.2. Simultaneous Improvement of LAI and WY Promotes Livestock Production

Current research tends to focus predominantly on the adverse impacts of climate warming on future livestock production while neglecting to explore the synergistic effects of enhanced water availability and grassland greening (Li et al., 2023; Zhang, M et al., 2023). This study seeks to address this gap by presenting a novel perspective, underscoring how the simultaneous and continuous growth in LAI and WY can be a catalyst for the advancement of livestock production within the evolving natural grazing environment. This is expected to affect the lives of more than 10 million pastoralists from socioeconomically disadvantaged backgrounds in NCTP (Ho, 2016).

Four provinces/autonomous regions (i.e., Inner Mongolia, Qinghai, Tibet, and Xinjiang) were selected to predict stocking numbers of herbivores (i.e., sheep and cattle) during the future period. During the historical period, ‘grazing exclusion’ was implemented in these regions to restore grassland ecosystems (Wang, L et al., 2018), as historical stocking numbers of herbivores showed a decreasing trend or a sharp variation (Figure 10). For the future period, stocking numbers of herbivores in the four provinces would increase at a higher rate under higher

carbon emission scenarios (Figure 10), which may result from higher increasing rates in both LAI and WY (Figure 6). In the four provinces, stocking numbers of herbivores increase first and then slightly decrease under the SSP126 scenario, whereas stocking numbers of herbivores continue to increase for the other two scenarios. Under the SSP245 scenario, stocking numbers of herbivores in Inner Mongolia are likely to increase to ~95 million by 2100, whereas stocking numbers of herbivores in the other three provinces are only likely to increase to 51–77 million. In addition, growth rates of predicted herbivore stocking numbers in 2100 compared to 2020 are largest in Qinghai Province (57%–538%), followed by Tibet (72%–514%), Xinjiang (23%–171%), and Inner Mongolia (19%–126%). This indicates that livestock production has the greatest potential to expand in Qinghai and Tibet in the future due to their faster increases in both LAI and WY, whereas the expansion of livestock production in Inner Mongolia may require more attention to the balance of grass and livestock.

4.3. Increased Water Use Efficiency Enhances the Sustainability of Regional Water Resources

Elevated CO₂ has been found to enhance the net carbon sink and WUE of grassland in a warming climate (Blumenthal et al., 2013; Morgan et al., 2011), aided by an increase in soil moisture, enhancing water availability (Liu, X et al., 2020) or an increase in root growth, improving nitrogen absorption efficiency (Roy et al., 2016). Field experiments over 21 years (Pastore et al., 2019) have shown that responses of grassland functional groups to elevated CO₂ can be quick and also persistent. However, it has also been observed that increasing seasonality in precipitation (e.g., increases in non-spring precipitation) may limit the above responses to elevated CO₂ (Hovenden et al., 2014, 2019), resulting in a decrease in biomass production and WUE. In most scenarios in our study (except for the SSP126 scenario for the PM ET_a scheme), LAI-induced increases in GPP are greater than LAI-induced increases in ET_a, resulting in increasing WUE (Figure 9b). Therefore, in the context of increasing precipitation, CO₂, and air temperature, grassland tends to consume water more efficiently to sustain its growth. Meanwhile, the differences between annual WY based on GPP-based ET_a and the other two ET_a schemes are significant (Figure 6), indicating that an increase in WUE is likely to improve the sustainability of local water resources.

4.4. Intensified Evaporation Recycling Contributes to Continuous Increases in Water Yield

Vegetation greening in ecological restoration regions often leads to regional water crises (Bai et al., 2020; Zhang, J et al., 2021; Zhao, M et al., 2021). However, the effect of grassland greening on WY in areas with large inter-annual variability in precipitation is more complicated (Hersbach et al., 2020; Li, J et al., 2017; Zhang, J et al., 2022). Widespread greening increases the water availability of local and downwind regions, when considering the influence of evaporation recycling (Cui et al., 2022; Teo et al., 2022). Meanwhile, positive feedbacks in terms of vegetation greening and evaporation recycling at micro and macro levels can reinforce one another (Te Wierik et al., 2021). In our study, intensified evaporation recycling is found to decrease ET_a by 4% in grassland areas under the SSP126 scenario (Figure 9c). Both local and upwind vegetation greening were estimated to have increased local precipitation by 1.2% (a globally averaged value) through evaporation recycling during 2001–2018 (Cui et al., 2022). Therefore, during the future period, intensified evaporation recycling may contribute to the continued increase in WY by increasing water supply and decreasing water demand.

5. Conclusion

This study analyzed the water resource availability across NCTP under grassland greening and climate warming during 1982–2100. By combining diagnostic (PM ET_a) and prognostic ET_a schemes (GPP-based ET_a and CMIP6-based ET_a), the effects of plant physiological factors and hydrological feedbacks on WY during the future period were discussed. Meanwhile, the influence of regional water resource availability and ongoing grassland greening on livestock production was first quantified. The main findings are summarized as follows.

1. The coexistence of grassland greening and enhanced water resource availability was observed in most of NCTP during the future period. Annual WY based on PM ET_a was the least sustainable scheme for regional water resources, followed by those based on CMIP6-based ET_a and GPP-based ET_a. Moreover, the water resource availability of three sub-regions has notable improvement, especially for regions I and III. However, there is a high likelihood that some regions will face water insecurity in the future, for example, Tian Shan, Qilian Shan, and the border of Ningxia and Inner Mongolia for region II. Additionally, the SSP585 scenario showed

- the most positive results for both grassland and regional water resources, whereas 2081–2100 (2051–2080) is the period of concern for the SSP126 (SSP245) scenario.
2. Positive influence of plant physiological factors (temperature, LAI, and WUE effects) and hydrological feedbacks (evaporation recycling) on WY in relation to climate warming, elevated CO₂ concentrations, and grassland greening were quantified. Enhanced atmospheric water transport, increased WUE, and intensified evaporation recycling across NCTP contribute to increased WY even with increased ET_a caused by grassland greening. An increase in WUE is found to result in a decrease in ET_a by up to 12% under the SSP126 scenario, while intensified evaporation recycling would also lead to a decrease in ET_a by 4% under the SSP126 scenario. Among plant physiological factors, an increase in ET_a caused by the temperature and LAI effects would be larger than a decrease in ET_a arising from the WUE effect.
 3. Continuous and synchronous increases in LAI and WY are expected to promote the development of livestock production, which may alleviate the restrictions imposed on grazing policies. Stocking numbers of herbivores in the four main provinces of NCTP would increase at a higher rate under higher carbon emission scenarios during the future period, corresponding to changes in WY and LAI. Qinghai and Tibet have the greatest potential for the expansion of livestock production in the future due to their faster increases in both LAI and WY, whereas the expansion of livestock production in Inner Mongolia may require more attention to the balance of grass and livestock.

Overall, this study explores the interactions among grassland greening, water resource availability, and livestock production, guiding adaptation strategies to improve water security across vast grasslands in drylands worldwide. The study also highlights the potential for expanded livestock production in areas where favorable water resources and grassland greening coexist, which could positively impact the lives of over 10 million pastoralists from socioeconomically disadvantaged backgrounds across NCTP region. The findings of this study have significant implications for policymakers and researchers working toward grassland and water resources management in arid and semi-arid regions.

Conflict of Interest

The authors declare no conflicts of interest relevant to this study.

Data Availability Statement

CMFD climatic forcing data are available in Yang et al., 2019. GLASS products (including LAI, ET_a, and GPP) are based on Liang et al. (2021) (can be accessed at <http://www.glass.umd.edu/>). GLOBMAP LAI is available in Liu, R et al. (2021). CLCD land cover data are available in Yang and Huang (2021). CMIP6 original projections are based on Eyring et al. (2016) (can be accessed at <https://esgf-node.llnl.gov/search/cmip6/>). GLEAM 3.5a and 3.5b ET_a are based on Martens et al. (2017) (can be accessed at <https://www.gleam.eu/>). PML ET_a is available in Zhang, Y Q (2020). AVHRR ET_a is based on Zhang et al. (2016), FLUXCOM ET_a is based on Jung et al. (2019), and BESS ET_a is based on Jiang and Ryu (2016) (accessed from <https://www.ntsg.umt.edu/project/global-et.php>, <https://www.bgc-jena.mpg.de/geodb/projects/Home.php>, and <https://www.environment.snu.ac.kr/bess-flux>, respectively). Key portions of the computer code used to process the results and develop the figures are available in Zhang and Long (2023).

References

- Allen, R. G., Pereira, L. S., Raes, D., & Smith, M. (1998). *Crop evapotranspiration: Guidelines for computing crop water requirements*. FAO. Retrieved from <https://www.fao.org/3/X0490E/x0490e00.htm>
- Bai, P., Liu, X., Zhang, Y., & Liu, C. (2020). Assessing the impacts of vegetation greenness change on evapotranspiration and water yield in China. *Water Resources Research*, 56(10), e2019WR027019. <https://doi.org/10.1029/2019WR027019>
- Bardgett, R. D., Bullock, J. M., Lavorel, S., Manning, P., Schaffner, U., Ostle, N., et al. (2021). Combatting global grassland degradation. *Nature Reviews Earth & Environment*, 2(10), 720–735. <https://doi.org/10.1038/s43017-021-00207-2>
- Bengtsson, J., Bullock, J. M., Egoh, B., Everson, C., Everson, T., O'connor, T., et al. (2019). Grasslands-more important for ecosystem services than you might think. *Ecosphere*, 10(2), e02582. <https://doi.org/10.1002/ecs2.2582>
- Blumenthal, D. M., Resco, V., Morgan, J. A., Williams, D. G., Lecain, D. R., Hardy, E. M., et al. (2013). Invasive forb benefits from water savings by native plants and carbon fertilization under elevated CO₂ and warming. *New Phytologist*, 200(4), 1156–1165. <https://doi.org/10.1111/nph.12459>
- Brun, F., Berthier, E., Wagnon, P., Kääh, A., & Treichler, D. (2017). A spatially resolved estimate of High Mountain Asia glacier mass balances from 2000 to 2016. *Nature Geoscience*, 10(9), 668–673. <https://doi.org/10.1038/ngeo2999>

Acknowledgments

This study was jointly supported by the Major Science and Technology Projects of Inner Mongolia Autonomous Region (2020ZD0009) and the National Natural Science Foundation of China (52325901, 52079065, and 52125901). The reviewers and editors' comments and efforts in improving this study are highly appreciated.

- Bryan, B. A., Gao, L., Ye, Y., Sun, X., Connor, J. D., Crossman, N. D., et al. (2018). China's response to a national land-system sustainability emergency. *Nature*, 559(7713), 193–204. <https://doi.org/10.1038/s41586-018-0280-2>
- Chen, C., Park, T., Wang, X., Piao, S., Xu, B., Chaturvedi, R. K., et al. (2019). China and India lead in greening of the world through land-use management. *Nature Sustainability*, 2(2), 122–129. <https://doi.org/10.1038/s41893-019-0220-7>
- Chen, Y., Li, Z., Fan, Y., Wang, H., & Deng, H. (2015). Progress and prospects of climate change impacts on hydrology in the arid region of northwest China. *Environmental Research*, 139, 11–19. <https://doi.org/10.1016/j.envres.2014.12.029>
- Chen, Z., & Wang, S. (2000). *Typical grassland ecosystem in China (in Chinese)*. Science Press. Retrieved from <https://book.sciencereading.cn/shop/book/Booksimple/show.do?id=%20BF717DC85CB85499CB3C264A255991D65000>
- Cui, J., Lian, X., Huntingford, C., Gimeno, L., Wang, T., Ding, J., et al. (2022). Global water availability boosted by vegetation-driven changes in atmospheric moisture transport. *Nature Geoscience*, 15(982–988), 982–988. <https://doi.org/10.1038/s41561-022-01061-7>
- Eyring, V., Bony, S., Meehl, G. A., Senior, C. A., Stevens, B., Stouffer, R. J., & Taylor, K. E. (2016). Overview of the coupled model intercomparison project phase 6 (CMIP6) experimental design and organization [dataset]. *Geoscientific Model Development*, 9(5), 1937–1958. <https://doi.org/10.5194/gmd-9-1937-2016>
- Fan, K., Zhang, Q., Li, J., Chen, D., & Xu, C.-Y. (2021). The scenario-based variations and causes of future surface soil moisture across China in the twenty-first century. *Environmental Research Letters*, 16(3), 034061. <https://doi.org/10.1088/1748-9326/abde5e>
- Gu, S., Tang, Y., Cui, X., Kato, T., Du, M., Li, Y., & Zhao, X. (2005). Energy exchange between the atmosphere and a meadow ecosystem on the Qinghai-Tibetan Plateau. *Agricultural and Forest Meteorology*, 129(3), 175–185. <https://doi.org/10.1016/j.agrformet.2004.12.002>
- Gudmundsson, L., Bremnes, J. B., Haugen, J. E., & Engen-Skaugen, T. (2012). Technical note: Downscaling RCM precipitation to the station scale using statistical transformations – A comparison of methods. *Hydrology and Earth System Sciences*, 16(9), 3383–3390. <https://doi.org/10.5194/hess-16-3383-2012>
- He, J., Yang, K., Tang, W., Lu, H., Qin, J., Chen, Y., & Li, X. (2020). The first high-resolution meteorological forcing dataset for land process studies over China [Dataset]. *Scientific Data*, 7(1), 25. <https://doi.org/10.1038/s41597-020-0369-y>
- Hersbach, H., Bell, B., Berrisford, P., Hirahara, S., Horányi, A., Muñoz-Sabater, J., et al. (2020). The ERA5 global reanalysis. *Quarterly Journal of the Royal Meteorological Society*, 146(730), 1999–2049. <https://doi.org/10.1002/qj.3803>
- Ho, P. (2016). Empty institutions, non-credibility and pastoralism: China's grazing ban, mining and ethnicity. *Journal of Peasant Studies*, 43(6), 1145–1176. <https://doi.org/10.1080/03066150.2016.1239617>
- Hoek Van Dijke, A. J., Herold, M., Mallick, K., Benedict, I., Machwitz, M., Schlerf, M., et al. (2022). Shifts in regional water availability due to global tree restoration. *Nature Geoscience*, 15(5), 363–368. <https://doi.org/10.1038/s41561-022-00935-0>
- Hovenden, M. J., Leuzinger, S., Newton, P. C. D., Fletcher, A., Faticchi, S., Lüscher, A., et al. (2019). Globally consistent influences of seasonal precipitation limit grassland biomass response to elevated CO₂. *Nature Plants*, 5(2), 167–173. <https://doi.org/10.1038/s41477-018-0356-x>
- Hovenden, M. J., Newton, P. C. D., & Wills, K. E. (2014). Seasonal not annual rainfall determines grassland biomass response to carbon dioxide. *Nature*, 511(7511), 583–586. <https://doi.org/10.1038/nature13281>
- Hugonnet, R., McNabb, R., Berthier, E., Menounos, B., Nuth, C., Girod, L., et al. (2021). Accelerated global glacier mass loss in the early twenty-first century. *Nature*, 592(7856), 726–731. <https://doi.org/10.1038/s41586-021-03436-z>
- Jiang, C., & Ryu, Y. (2016). Multi-scale evaluation of global gross primary productivity and evapotranspiration products derived from Breathing Earth System Simulator (BESS) [Dataset]. *Remote Sensing of Environment*, 186, 528–547. <https://doi.org/10.1016/j.rse.2016.08.030>
- Jiang, P., Ding, W.-g., Yuan, Y., Hu, L., & Ye, W. (2022). Identifying trend shifts in vegetation greenness in China from 1982 to 2015. *Land Degradation & Development*, 33(9), 1434–1445. <https://doi.org/10.1002/ldr.4240>
- Jung, M., Koirala, S., Weber, U., Ichii, K., Gans, F., Camps-Valls, G., et al. (2019). The FLUXCOM ensemble of global land-atmosphere energy fluxes [Dataset]. *Scientific Data*, 6(1), 74. <https://doi.org/10.1038/s41597-019-0076-8>
- Kustas, W. P., Choudhury, B. J., Moran, M. S., Reginato, R. J., Jackson, R. D., Gay, L. W., & Weaver, H. L. (1989). Determination of sensible heat flux over sparse canopy using thermal infrared data. *Agricultural and Forest Meteorology*, 44(3), 197–216. [https://doi.org/10.1016/0168-1923\(89\)90017-8](https://doi.org/10.1016/0168-1923(89)90017-8)
- Kustas, W. P., & Norman, J. M. (1999). Evaluation of soil and vegetation heat flux predictions using a simple two-source model with radiometric temperatures for partial canopy cover. *Agricultural and Forest Meteorology*, 94(1), 13–29. [https://doi.org/10.1016/S0168-1923\(99\)00005-2](https://doi.org/10.1016/S0168-1923(99)00005-2)
- Lan, X., Liu, Z., Chen, X., Lin, K., & Cheng, L. (2021). Trade-off between carbon sequestration and water loss for vegetation greening in China. *Agriculture, Ecosystems & Environment*, 319, 107522. <https://doi.org/10.1016/j.agee.2021.107522>
- Lemaire, G., Hodgson, J., & Chabbi, A. (2011). *Grassland productivity and ecosystem services* (pp. 1–287). CABI. <https://doi.org/10.1079/9781845938093.0000>
- Lhomme, J. P., Chehbouni, A., & Monteny, B. (2000). Sensible heat flux-radiometric surface temperature relationship over sparse vegetation: Parameterizing B-1. *Boundary-Layer Meteorology*, 97(3), 431–457. <https://doi.org/10.1023/A:1002786402695>
- Li, C., Fu, B., Wang, S., Stringer, L. C., Wang, Y., Li, Z., et al. (2021). Drivers and impacts of changes in China's drylands. *Nature Reviews Earth & Environment*, 2(12), 858–873. <https://doi.org/10.1038/s43017-021-00226-z>
- Li, C., Fu, B., Wang, S., Stringer, L. C., Zhou, W., Ren, Z., et al. (2023). Climate-driven ecological thresholds in China's drylands modulated by grazing. *Nature Sustainability*, 6(11), 1363–1372. <https://doi.org/10.1038/s41893-023-01187-5>
- Li, J., Liu, D., Wang, T., Li, Y., Wang, S., Yang, Y., et al. (2017). Grassland restoration reduces water yield in the headstream region of Yangtze River. *Scientific Reports*, 7(1), 2162. <https://doi.org/10.1038/s41598-017-02413-9>
- Li, L., Chen, J., Han, X., Zhang, W., & Shao, C. (2020). Major regional grasslands in China. In L. Li, J. Chen, X. Han, W. Zhang, & C. Shao (Eds.), *Grassland ecosystems of China: A synthesis and resume* (pp. 81–120). Springer Singapore. https://doi.org/10.1007/978-981-15-3421-8_4
- Li, Y., Su, F., Chen, D., & Tang, Q. (2019). Atmospheric water transport to the endorheic Tibetan plateau and its effect on the hydrological status in the region. *Journal of Geophysical Research: Atmospheres*, 124(23), 12864–12881. <https://doi.org/10.1029/2019JD031297>
- Liang, S., Cheng, J., Jia, K., Jiang, B., Liu, Q., Xiao, Z., et al. (2021). The global land surface satellite (GLASS) product suite [dataset]. *Bulletin of the American Meteorological Society*, 102(2), E323–E337. <https://doi.org/10.1175/BAMS-D-18-0341.1>
- Liu, R., Liu, Y., & Chen, J. (2021). GLOBMAP global leaf area index since 1981 [dataset]. Zenodo. <https://zenodo.org/record/4700264#.Y1uiz8tBzDC>
- Liu, X., Feng, X., & Fu, B. (2020). Changes in global terrestrial ecosystem water use efficiency are closely related to soil moisture. *Science of the Total Environment*, 698, 134165. <https://doi.org/10.1016/j.scitotenv.2019.134165>
- Liu, Y., Liu, R., & Chen, J. M. (2012). Retrospective retrieval of long-term consistent global leaf area index (1981–2011) from combined AVHRR and MODIS data [Dataset]. *Journal of Geophysical Research*, 117(G4), G04003. <https://doi.org/10.1029/2012JG002084>
- Lu, F., Hu, H. F., Sun, W. J., Zhu, J. J., Liu, G. B., Zhou, W. M., et al. (2018). Effects of national ecological restoration projects on carbon sequestration in China from 2001 to 2010. *Proceedings of the National Academy of Sciences*, 115(16), 4039–4044. <https://doi.org/10.1073/pnas.1700294115>

- Lu, J., Wang, G., Li, S., Feng, A., Zhan, M., Jiang, T., et al. (2021). Projected land evaporation and its response to vegetation greening over China under multiple scenarios in the CMIP6 models. *Journal of Geophysical Research: Biogeosciences*, 126(9), e2021JG006327. <https://doi.org/10.1029/2021JG006327>
- Luo, Y., Wang, X., Piao, S., Sun, L., Ciais, P., Zhang, Y., et al. (2018). Contrasting streamflow regimes induced by melting glaciers across the Tien Shan – Pamir – North Karakoram. *Scientific Reports*, 8(1), 16470. <https://doi.org/10.1038/s41598-018-34829-2>
- Maina, F. Z., Kumar, S. V., Albergel, C., & Mahanama, S. P. (2022). Warming, increase in precipitation, and irrigation enhance greening in High Mountain Asia. *Communications Earth & Environment*, 3(1), 43. <https://doi.org/10.1038/s43247-022-00374-0>
- Martens, B., Miralles, D. G., Lievens, H., Van Der Schalie, R., De Jeu, R. A. M., Fernández-Prieto, D., et al. (2017). GLEAM v3: Satellite-based land evaporation and root-zone soil moisture [dataset]. *Geoscientific Model Development*, 10(5), 1903–1925. <https://doi.org/10.5194/gmd-10-1903-2017>
- Miao, L., Sun, Z., Ren, Y., Schierhorn, F., & Müller, D. (2021). Grassland greening on the Mongolian Plateau despite higher grazing intensity. *Land Degradation & Development*, 32(2), 792–802. <https://doi.org/10.1002/ldr.3767>
- Miao, L. J., Li, S. Y., Zhang, F., Chen, T. X., Shan, Y. P., & Zhang, Y. S. (2020). Future drought in the dry lands of Asia under the 1.5 and 2.0 degrees C warming scenarios. *Earth's Future*, 8(6), e2019EF001337. <https://doi.org/10.1029/2019EF001337>
- Morgan, J. A., Lecain, D. R., Pendall, E., Blumenthal, D. M., Kimball, B. A., Carrillo, Y., et al. (2011). C4 grasses prosper as carbon dioxide eliminates desiccation in warmed semi-arid grassland. *Nature*, 476(7359), 202–205. <https://doi.org/10.1038/nature10274>
- Niu, Q., Xiao, X., Zhang, Y., Qin, Y., Dang, X., Wang, J., et al. (2019). Ecological engineering projects increased vegetation cover, production, and biomass in semiarid and subhumid Northern China. *Land Degradation & Development*, 30(13), 1620–1631. <https://doi.org/10.1002/ldr.3351>
- Pastore, M. A., Lee, T. D., Hobbie, S. E., & Reich, P. B. (2019). Strong photosynthetic acclimation and enhanced water-use efficiency in grassland functional groups persist over 21 years of CO₂ enrichment, independent of nitrogen supply. *Global Change Biology*, 25(9), 3031–3044. <https://doi.org/10.1111/gcb.14714>
- Piao, S., Wang, X., Park, T., Chen, C., Lian, X., He, Y., et al. (2020). Characteristics, drivers and feedbacks of global greening. *Nature Reviews Earth & Environment*, 1(1), 14–27. <https://doi.org/10.1038/s43017-019-0001-x>
- Pilgrim, D. H., Chapman, T. G., & Doran, D. G. (1988). Problems of rainfall-runoff modelling in arid and semiarid regions. *Hydrological Sciences Journal*, 33(4), 379–400. <https://doi.org/10.1080/0266668809491261>
- Purdy, A. J., Fisher, J. B., Goulden, M. L., & Famiglietti, J. S. (2016). Ground heat flux: An analytical review of 6 models evaluated at 88 sites and globally. *Journal of Geophysical Research: Biogeosciences*, 121(12), 3045–3059. <https://doi.org/10.1002/2016JG003591>
- Roy, J., Picon-Cochard, C., Augusti, A., Benot, M.-L., Thiery, L., Darsonville, O., et al. (2016). Elevated CO₂ maintains grassland net carbon uptake under a future heat and drought extreme. *Proceedings of the National Academy of Sciences*, 113(22), 6224–6229. <https://doi.org/10.1073/pnas.1524527113>
- Skelton, R. P., West, A. G., & Dawson, T. E. (2015). Predicting plant vulnerability to drought in biodiverse regions using functional traits. *Proceedings of the National Academy of Sciences*, 112(18), 5744–5749. <https://doi.org/10.1073/pnas.1503376112>
- Su, B., Huang, J., Mondal, S. K., Zhai, J., Wang, Y., Wen, S., et al. (2021). Insight from CMIP6 SSP-RCP scenarios for future drought characteristics in China. *Atmospheric Research*, 250, 105375. <https://doi.org/10.1016/j.atmosres.2020.105375>
- Su, Y., Guo, Q., Hu, T., Guan, H., Jin, S., An, S., et al. (2020). An updated vegetation map of China (1:1000000). *Science Bulletin*, 65(13), 1125–1136. <https://doi.org/10.1016/j.scib.2020.04.004>
- Teo, H. C., Raghavan, S. V., He, X., Zeng, Z., Cheng, Y., Luo, X., et al. (2022). Large-scale reforestation can increase water yield and reduce drought risk for water-insecure regions in the Asia-Pacific. *Global Change Biology*, 28(21), 6385–6403. <https://doi.org/10.1111/gcb.16404>
- Te Wierik, S. A., Cammeraat, E. L. H., Gupta, J., & Artzy-Randrup, Y. A. (2021). Reviewing the impact of land use and land-use change on moisture recycling and precipitation patterns. *Water Resources Research*, 57(7), e2020WR029234. <https://doi.org/10.1029/2020WR029234>
- Wang, L., Gan, Y., Wiesmeier, M., Zhao, G., Zhang, R., Han, G., et al. (2018). Grazing exclusion—An effective approach for naturally restoring degraded grasslands in northern China. *Land Degradation & Development*, 29(12), 4439–4456. <https://doi.org/10.1002/ldr.3191>
- Wang, X., Zhang, B., Li, F., Li, X., Li, X., Wang, Y., et al. (2021). Vegetation restoration projects intensify intraregional water recycling processes in the agro-pastoral ecotone of northern China. *Journal of Hydrometeorology*, 22(6), 1385–1403. <https://doi.org/10.1175/JHM-D-20-0125.1>
- Witte, J. P. M., Kruijt, B., & Maas, C. (2006). *The effects of rising CO₂ levels on evapotranspiration, Kiwa rapport KWR 06.004*. Nieuwegein. Retrieved from <https://www.semanticscholar.org/paper/The-effects-of-rising-CO2-levels-on-Kwr/c8f87aaae609a4aed9ae92bf4558ac390bcadd#citing-papers>
- Wood, A. W., Leung, L. R., Sridhar, V., & Lettenmaier, D. P. (2004). Hydrologic implications of dynamical and statistical approaches to downscaling climate model outputs. *Climatic Change*, 62(1), 189–216. <https://doi.org/10.1023/B:CLIM.0000013685.99609.9e>
- Xiao, Z., Liang, S., Wang, J., Xiang, Y., Zhao, X., & Song, J. (2016). Long-time-series global land surface satellite leaf area index product derived from MODIS and AVHRR surface reflectance [dataset]. *IEEE Transactions on Geoscience and Remote Sensing*, 54(9), 5301–5318. <https://doi.org/10.1109/TGRS.2016.2560522>
- Yang, J., & Huang, X. (2021). The 30 m annual land cover dataset and its dynamics in China from 1990 to 2019 [Dataset]. *Earth System Science Data*, 13(8), 3907–3925. <https://doi.org/10.5194/essd-13-3907-2021>
- Yang, K., He, J., Tang, W., Lu, H., Qin, J., Chen, Y., et al. (2019). China meteorological forcing dataset (1979–2018) [Dataset]. A big Earth data platform for three poles. *Atmospheric Physics*. <https://doi.org/10.11888/AtmosphericPhysics.tpe.249369.file>
- Yilmaz, M. T., Anderson, M. C., Zaitchik, B., Hain, C. R., Crow, W. T., Ozdogan, M., et al. (2014). Comparison of prognostic and diagnostic surface flux modeling approaches over the Nile. *River basin*, 50(1), 386–408. <https://doi.org/10.1002/2013WR014194>
- Yu, L., Xue, Y., & Diallo, I. (2021). Vegetation greening in China and its effect on summer regional climate. *Science Bulletin*, 66(1), 13–17. <https://doi.org/10.1016/j.scib.2020.09.003>
- Zeng, Z., Piao, S., Li, L. Z. X., Wang, T., Ciais, P., Lian, X., et al. (2018). Impact of Earth greening on the terrestrial water cycle. *Journal of Climate*, 31(7), 2633–2650. <https://doi.org/10.1175/JCLI-D-17-0236.1>
- Zhang, C., & Long, D. (2023). Supplementary code to: Grassland greening and water resource availability may coexist in a warming climate. *Zenodo*. <https://zenodo.org/record/7739861>
- Zhang, C., Long, D., Zhang, Y., Anderson, M. C., Kustas, W. P., & Yang, Y. (2021). A decadal (2008–2017) daily evapotranspiration data set of 1 km spatial resolution and spatial completeness across the North China Plain using TSEB and data fusion. *Remote Sensing of Environment*, 262, 112519. <https://doi.org/10.1016/j.rse.2021.112519>
- Zhang, J., Zhang, Y., Sun, G., Song, C., Dannenberg, M. P., Li, J., et al. (2021). Vegetation greening weakened the capacity of water supply to China's South-to-North Water Diversion Project. *Hydrology and Earth System Sciences*, 25(10), 5623–5640. <https://doi.org/10.5194/hess-25-5623-2021>

- Zhang, J., Zhang, Y., Sun, G., Song, C., Li, J., Hao, L., & Liu, N. (2022). Climate variability masked greening effects on water yield in the Yangtze river basin during 2001–2018. *Water Resources Research*, *58*(1), e2021WR030382. <https://doi.org/10.1029/2021WR030382>
- Zhang, K., Kimball, J. S., Nemani, R. R., & Running, S. W. (2010). A continuous satellite-derived global record of land surface evapotranspiration from 1983 to 2006 [Dataset]. *Water Resources Research*, *46*(9), W09522. <https://doi.org/10.1029/2009WR008800>
- Zhang, M., Delgado-Baquerizo, M., Li, G., Isbell, F., Wang, Y., Hautier, Y., et al. (2023). Experimental impacts of grazing on grassland biodiversity and function are explained by aridity. *Nature Communication*, *14*(1), 5040. <https://doi.org/10.1038/s41467-023-40809-6>
- Zhang, Y., Gentile, P., Luo, X., Lian, X., Liu, Y., Zhou, S., et al. (2022). Increasing sensitivity of dryland vegetation greenness to precipitation due to rising atmospheric CO₂. *Nature Communications*, *13*(1), 4875. <https://doi.org/10.1038/s41467-022-32631-3>
- Zhang, Y. Q. (2020). PML_V2 global evapotranspiration and gross primary production (2002.07–2019.08). National Tibetan Plateau [Dataset]. Third Pole Environment Data Center. <https://doi.org/10.11888/Geogra.tpcdc.270251>
- Zhang, Y. Q., Pena-Arancibia, J. L., Mcvigar, T. R., Chiew, F. H. S., Vaze, J., Liu, C. M., et al. (2016). Multi-decadal trends in global terrestrial evapotranspiration and its components [Dataset]. *Scientific Reports*, *6*(1), 19124. <https://doi.org/10.1038/srep19124>
- Zhao, M., Zhang, J., Velicogna, I., Liang, C., & Li, Z. (2021). Ecological restoration impact on total terrestrial water storage. *Nature Sustainability*, *4*(1), 56–62. <https://doi.org/10.1038/s41893-020-00600-7>
- Zhao, W., Hu, Z., Guo, Q., Wu, G., Chen, R., & Li, S. (2020). Contributions of climatic factors to interannual variability of the vegetation index in northern China grasslands. *Journal of Climate*, *33*(1), 175–183. <https://doi.org/10.1175/JCLI-D-18-0587.1>
- Zhou, S., Williams, A. P., Lintner, B. R., Berg, A. M., Zhang, Y., Keenan, T. F., et al. (2021). Soil moisture–atmosphere feedbacks mitigate declining water availability in drylands. *Nature Climate Change*, *11*(1), 38–44. <https://doi.org/10.1038/s41558-020-00945-z>
- Zhu, Z., Piao, S., Myneni, R. B., Huang, M., Zeng, Z., Canadell, J. G., et al. (2016). Greening of the Earth and its drivers. *Nature Climate Change*, *6*(8), 791–795. <https://doi.org/10.1038/nclimate3004>

References From the Supporting Information

- Adler, R. F., Huffman, G. J., Chang, A., Ferraro, R., Xie, P.-P., Janowiak, J., et al. (2003). The version-2 global precipitation climatology project (GPCP) monthly precipitation analysis (1979–present) [dataset]. *Journal of Hydrometeorology*, *4*(6), 1147–1167. [https://doi.org/10.1175/1525-7541\(2003\)004<1147:tvGPCP>2.0.CO;2](https://doi.org/10.1175/1525-7541(2003)004<1147:tvGPCP>2.0.CO;2)
- Gelaro, R., McCarty, W., Suárez, M. J., Todling, R., Molod, A., Takacs, L., et al. (2017). The modern-era retrospective analysis for research and applications, version 2 (MERRA-2) [dataset]. *Journal of Climate*, *30*(14), 5419–5454. <https://doi.org/10.1175/JCLI-D-16-0758.1>
- Harris, I., Osborn, T. J., Jones, P., & Lister, D. (2020). Version 4 of the CRU TS monthly high-resolution gridded multivariate climate dataset [Dataset]. *Scientific Data*, *7*(1), 109. <https://doi.org/10.1038/s41597-020-0453-3>
- Li, M., Wu, P., Ma, Z., Pan, Z., Lv, M., Yang, Q., & Duan, Y. (2022). The increasing role of vegetation transpiration in soil moisture loss across China under global warming. *Journal of Hydrometeorology*, *23*(2), 253–274. <https://doi.org/10.1175/JHM-D-21-0132.1>
- Ma, Y., Hu, Z., Xie, Z., Ma, W., Wang, B., Chen, X., et al. (2020). A long-term (2005–2016) dataset of hourly integrated land–atmosphere interaction observations on the Tibetan Plateau [Dataset]. *Earth System Science Data*, *12*(4), 2937–2957. <https://doi.org/10.5194/essd-12-2937-2020>